GBT-Based Buckling Analysis of Thin-Walled Steel Frames with Semi-Rigid Joints

Enio Mesacasa Jr.[1], Cilmar Basaglia[2], Dinar Camotim[3], Maximiliano Malite[1]

Abstract

This paper presents and discusses the available results of an ongoing investigation concerning the use of Generalized Beam Theory (GBT) to analyze the local, distortional and global buckling behavior of thin-walled steel frames with semi-rigid joints. Initially, an overview of the concepts and procedures involved in performing a GBT frame buckling analysis is provided, paying particular attention to the aspects related to ensuring displacement compatibility at the frame joints (between the end cross-sections of non-aligned members). Next, in a first attempt to simulate a frame joint semi-rigidity, linear spring elements, characterized by their stiffness values and relating the appropriate generalized displacements of the converging member end cross-sections, are incorporated into the buckling analysis. Finally, in order to illustrate the application and assess the merits of the above approach to modeling semi-rigid joints, numerical results concerning the buckling behavior of simple L-shaped and portal plane frames are presented and discussed. The frames analyzed (i) are formed by plain and lipped I-section members, (ii) are acted by loadings causing axial compression and in-plane (major-axis) bending, and (iii) exhibit rotational springs at the joints, involving exclusively in-plane bending. The influence of the spring stiffness, which alters the member bending moment diagrams, on the frame buckling behavior (critical buckling load and mode nature) is investigated. For validation purposes, some GBT buckling results are compared with values obtained from ANSYS shell finite element analyses.

1. Introduction

The extensive application of thin-walled steel frames (*e.g.*, cold-formed ones) in the construction industry stems mostly from their high structural efficiency (large strength-to-weight ratio), remarkable fabrication versatility and very easy/speedy erection. Such frames are often formed by members (columns, beams or beam-columns) with very slender open cross-sections, invariably exhibiting very low torsional stiffness and strong susceptibility to local, distortional and global deformations, which makes the grasp and assessment of all the aspects involved in their structural response a formidable task. It requires a combination of (i) carefully planned and executed experimental investigations, such as those reported by Dubina (2008) or Zhang & Rasmussen (2014), and (ii) rigorous numerical analyses,

---

[1] SET-EESC, Engineering School of São Carlos, Univ. of São Paulo <enio.mesacasa@gmail.com; mamalite@sc.usp.br>
[2] Dept. of Structural Engineering, School of Civil Eng. and Arch., Univ. of Campinas <cbasaglia@fec.unicamp.br>
[3] CERIS, ICIST, DECivil, Instituto Superior Técnico, Universidade de Lisboa, <dcamotim@civil.ist.utl.pt>

performed by means of sophisticated shell and/or solid finite element models that often require using very elaborated computational resources (*e.g.*, contact formulations intended to simulate realistically joints or complex support and bracing conditions). Naturally, financial costs severely restrict the performance of frame tests, mainly used to provide benchmarks for the validation and calibration of numerical models. On the other hand, the routine use of rigorous numerical analyses is still prohibitive for routine design applications, essentially because it consists of a highly time-consuming and computer-intensive approach (including data pre-processing and result post-processing) that also requires a strong command of nonlinear structural analysis concepts. This explains why virtually all the existing specifications for cold-formed steel structures (*e.g.*, AISI 2012) promote a "traditional" design approach. It combines (i) a frame global analysis, to obtain internal force and moment diagrams (possibly including frame second-order effects), with (ii) joint and member safety checks, where the latter include provisions associated with all possible cross-section (local/distortional) and member (global) instability phenomena.

In view of what was mentioned in the previous paragraph, it is just natural for the technical-scientific community working with cold-formed steel structures to be longing for a computational tool that (i) is based on beam models and (ii) is able to analyze thin-walled frames. Naturally, such beam models must necessarily be "advanced", in the sense that are required to capture phenomena associated with the occurrence of fairly arbitrary cross-section in-plan and out-of-plane deformations. Although beam models with those characteristics are available, the major difficulty concerning its use to analyze thin-walled frames resides in the appropriate treatment of joints – this is why the application of those models is practically always restricted to isolated members. Even in the context of frame global buckling analysis, which only requires handling the joint transmission of the torsion warping (*e.g.*, Trahair 1993, Basaglia *et al.* 2008, 2012 , Shayan & Rasmussen, 2014), the treatment of joints is far from easy and has only been achieved for a few joint configurations and connected member cross-section shapes. When local and distortional deformation are also taken into account, the problem becomes even more complex, since compatibility between the warping and transverse (membrane and flexural) displacements the connected member end cross-sections must be ensured (Basaglia *et al.* 2009, Camotim *et al.* 2010).

A very promising approach enabling the use of advanced beam finite elements to analyze the buckling and post-buckling behavior of thin-walled frames is Generalized Beam Theory (GBT), a beam theory incorporating genuine folded-plate concepts originally proposed by Schardt (1989), in the context of the buckling analysis of isolated members. GBT was recently applied to analyze the buckling and post-buckling behavior of structural systems, namely frames (mostly) and trusses – concerning the buckling analysis, the works of Camotim *et al.* (2010), Basaglia *et al.* (2010), and Basaglia & Camotim (2015) should be mentioned. Of course, the above applications involved structural systems built from members with only a few cross-section shapes and exhibiting specific joint configurations – those for which kinematic models are available. The establishment of a methodology for the development of such models in the context of (more or less) arbitrary cross-section shapes and joint configurations is an indispensable step before the GBT approach to analyze the buckling behavior of thin-walled structural systems can become a viable alternative for the wide and routine use by cold-formed steel designers.

It is still worth mentioning that an alternative approach to analyze thin-walled frames (buckling and post-buckling behavior) is been pursued at the University of Sydney by Rasmussen and his co-workers (Zhang *et al.* 2015a,b, Rasmussen *et al.* 2016). In essence, it consists of performing global frame analyses that take into account, indirectly, the local and/or distortional buckling effects through the "weakening" of the member material behavior. Obviously, the difficulties associated with the appropriate treatment of joints are the same faced by the researchers using GBT.

Up to now, GBT beam finite elements have already been shown to provide accurate and structurally illumination buckling solutions for plane and space thin-walled steel frames exhibiting a few combinations of joint configuration and connected member cross-section shape, and fairly general loading and support conditions (Camotim *et al.* 2010, Basaglia & Camotim 2010, 2015). However, all the structural systems analyzed had either rigid (frames) or pinned (trusses) joints. In the first case, it is assumes that the joints possess enough stiffness to allow for frame pre-buckling and buckling analyses based on full continuity (transmission) of internal forces and moments, namely the bending moments (M_j), as illustrated in Fig. 1(a). In the case of pinned joints, on the other hand, the performance of GBT buckling analyses seems to be straightforward, as shown by Basaglia & Camotim (2011, 2015) for steel trusses. The pinned member behaves as simply supported (joint with null bending stiffness), *i.e.*, independently from the remaining connected member(s), as illustrated in Fig. 1(c), showing a pinned joint connecting a beam to a continuous column. However, it is well known that the vast majority of steel structural system joints exhibit a finite (intermediate) stiffness, associated with the so-called semi-rigid joint behavior, depicted in Fig. 1(b). To the authors' best knowledge, GBT has never been employed to analyze the buckling behavior of frames with semi-rigid joints and, therefore, the objective of this work is to provide a first contribution towards its extension to handle this type of frames. At this stage, only simple plane frames are considered and the joint semi-rigid behavior, modeled by means of elastic springs, is restricted to in-plane bending.
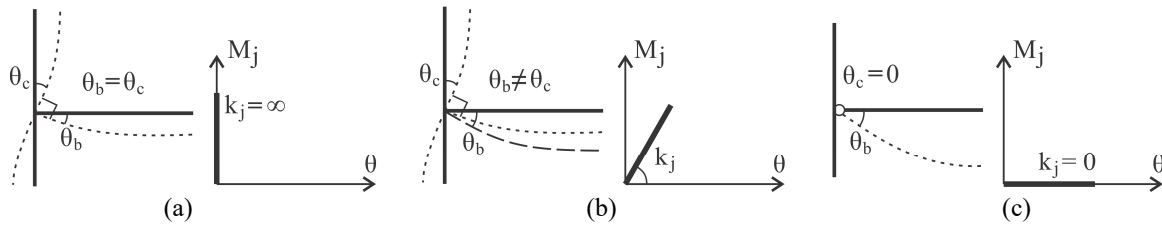

Figure 1: Behavior and (linear elastic) modeling of (a) rigid, (b) semi-rigid, and (c) pinned beam-to-column joints.

The paper presents and discusses the available results of an ongoing investigation aimed at applying GBT to assess the local, distortional and global buckling behavior of thin-walled steel frames with semi-rigid joints. These results concern simple L-shaped and portal plane frames formed by members with plain or lipped I cross-sections. As mentioned above, the joint semi-rigidity involves exclusively in-plane bending – major-axis bending in this case. In order to illustrate the capabilities of the GBT-based analyses, the frame geometries and loadings are selected to ensure the occurrence of critical local, distortional and global buckling. For validation purposes, most GBT buckling results are compared with values obtained from rigorous ANSYS (SAS 2009) shell finite element analyses.

2. Generalized Beam Theory (GBT) − Overview and Joint Semi-Rigidity
The main distinctive feature of GBT is the fact that the cross-section displacement field is expressed as a linear combination of structurally meaningful deformation modes (involving the whole cross-section). This feature makes it possible (i) to reduce considerably the number of degrees of freedom (DOFs) required to analyze a given structural system, (ii) to write the corresponding differential equilibrium equation system in a very convenient form (the coupling between the equations is minimized), and (iii) to obtain modal solutions providing in-depth insight on the mechanics of the problem under consideration. The performance of a GBT buckling analysis involves two main tasks: (i) a cross-section analysis, to identify the deformation modes and evaluate the associated modal mechanical properties, and (ii) a buckling analysis, consisting of the solution of a (modal) eigenvalue problem to obtain the buckling load parameters and associated mode shapes. Each of these two tasks will be addressed briefly next.

2.1 Cross-Section Analysis

Consider a prismatic thin-walled member a supposedly arbitrary branched (*n-walled*) open cross-section, as depicted in Fig. 2, which displays also the adopted global (X-Y-Z) and local/wall (*x-s-z*) coordinate systems (X and x are parallel to the member axis) – the wall displacements (*u-v-w*) are also indicated. In order to obtain a displacement field representation compatible with the classical beam theories, the components *u(x,s)*, *v(x,s)* and *w(x,s)* are expressed as

$$u(x,s) = u_k(s)\phi_{k,x}(x) \qquad v(x,s) = v_k(s)\phi_k(x) \qquad w(x,s) = w_k(s)\phi_k(x) \tag{1}$$

where (i) $(\phi)_{,x} \equiv d\phi/dx$, (ii) the summation convention applies to subscript k, (iii) functions $u_k(s)$, $v_k(s)$ and $w_k(s)$ are the cross-section deformation mode components, satisfying Vlasov's null membrane shear strain and transverse extension hypotheses ($\gamma_{xs}^M = \varepsilon_{ss}^M = 0$), and (iv) $\phi_k(x) \equiv \phi_k(X)$ are functions providing the deformation mode amplitude longitudinal variation (Silvestre & Camotim 2002, Dinis *et al.* 2006).

In this work, the cross-section analyses are performed following the procedure originally developed by Dinis *et al.* (2006) for arbitrarily branched open cross-sections. Figs. 3(a)-(b) show the cross-section geometries considered in this work (lipped and plain I-sections sharing the same web and flanges) and the corresponding GBT discretizations adopted, which involve either (i) two intermediate nodes in the web and one intermediate node per flange and lip (lipped I-section) or (ii) three intermediate nodes in the web and one intermediate node per flange (plain I-section). These discretizations lead to 22 and 19 deformation modes, respectively for the lipped and plain I-sections: 4 global, 4 distortional and either 14 or 11 local modes. Figs. 3(c)-(d) modes.
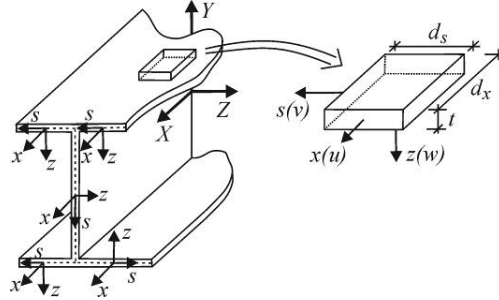

Figure 2: Arbitrary prismatic open-section thin-walled member and adopted coordinate axes and displacements
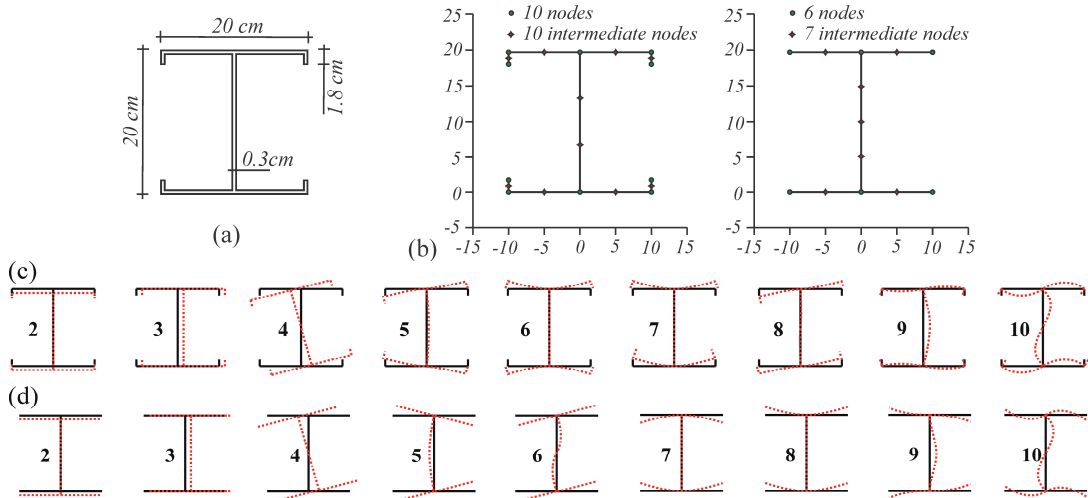

Figure 3: Lipped and plain I-section (a) dimensions, (b) GBT discretizations and (c)-(d) **2-10** deformation mode shapes.

4

2.2 Member Analysis – Finite Element Formulation

Once the deformation modes are known, the GBT differential equilibrium equation system defining the buckling eigenvalue problem to be solved can be established (Bebiano *et al.* 2007, Camotim *et al.* 2010),

$$C_{ik}\,\phi_{k,xxxx} - D_{ik}\,\phi_{k,xx} + B_{ik}\,\phi_k - \lambda\left[X^{\sigma}_{jik}\left(W_j^0\,\phi_{k,x}\right)_{,x} - X^{\tau}_{jki}\left(W_{j,x}^0\,\phi_k\right)_{,x} + W_{j,x}^0 X^{\tau}_{jik}\,\phi_{k,x}\right] = 0$$

$$W_j^0 = C_{jj}\,\phi_{j,xx}^0$$

(2)

where (i) λ is the load parameter, (ii) C_{ik}, D_{ik} and B_{ik} are cross-section modal mechanical properties obtained from the cross-section analysis (while C_{ik} and D_{ik} concern the warping displacements and torsional rotations, B_{ik} stems from local deformations), (iii) X^{σ}_{jik} and X^{τ}_{jik} are geometric stiffness matrices, whose are determined using the pre-buckling longitudinal normal stress resultants W_j^0 (axial force and/or bending moments) and shear stresses due to the normal stress gradients caused by non-uniform bending. The components of these matrices/tensors are given by

$$B_{ik} = \frac{E}{12(1-v^2)}\int_s t^3 w_{i,ss}w_{k,ss}ds$$

(3)

$$C_{ik} = E\int_s t\,u_iu_k\,ds + \frac{E}{12(1-v^2)}\int_s t^3 w_i w_k\,ds$$

(4)

$$D_{ik} = \frac{G\,t^3}{3}\int_s w_{i,s}w_{k,s}ds - \frac{v\,E\,t^3}{12(1-v^2)}\int_s \left(w_i\,w_{k,ss} + w_k\,w_{i,ss}\right)ds$$

(5)

$$X^{\sigma}_{jik} = \frac{E\,t}{C_{jj}}\int_s u_j\left(v_i\,v_k + w_i\,w_k\right)ds \qquad X^{\tau}_{jik} = \frac{E}{C_{jj}}\int_s F_j(s)\,w_{i,s}\,w_k\,ds$$

(6)

where (i) E, G and v are the material Young's modulus, shear modulus and Poisson's ratio, (ii) $F_j(s)$ is either the cross-section first moment of (ii₁) the area with respect to its major/minor axis ($j=2$ or 3) or (ii₂) the sectorial area with respect to the shear centre ($j=4$).

The solution of the buckling eigenvalue problem defined by for Eq. (2) is obtained by means of the GBT-based beam finite element formulation first proposed by Silvestre & Camotim (2003), in the context of FRP pultruded composite columns, and later enhanced by Bebiano *et al.* (2007) to account for the influence of the shear stresses caused by non-uniform bending. The 2-node finite element has $2n$ DOFs, where n is the number of GBT deformation modes included in the analysis, and Hermite cubic polynomials $\psi_i(x)$ are employed to approximate the mode amplitude functions $\phi_k(x)$,

$$\phi_k(x) = \psi_1(x)Q_{k1} + \psi_2(x)Q_{k2} + \psi_3(x)Q_{k3} + \psi_4(x)Q_{k4}$$

(7)

where $Q_{k1}=\phi_{k,x}(0)$, $Q_{k2}=\phi_k(0)$, $Q_{k3}=\phi_{k,x}(L_e)$, $Q_{k4}=\phi_k(L_e)$, where L_e is the finite element length. Making $\xi=x/L_e$, the above polynomials read

$$\psi_1(\xi) = L_e(\xi^3 - 2\xi^2 + \xi)$$

(8)

$$\psi_2(\xi) = 2\xi^3 - 3\xi^2 + 1$$

(9)

$$\psi_3(\xi) = L_e(\xi^3 - 2\xi^2)$$

(10)

$$\psi_4(\xi) = 3\xi^2 - 2\xi^3$$

(11)

Assuming that the longitudinal stress resultants concerning deformation modes **2** and **3** can be written as

$$W_j^0 = W_{0j}^0 + W_{1j}^0 \xi + W_{2j}^0 \xi^2 + W_{3j}^0 \xi^3 \tag{12}$$

which corresponds to an arbitrary cubic bending moment diagram (see Fig. 4), the finite element linear stiffness ($[K_e]$) and geometric stiffness ($[G_e]$) are of the form
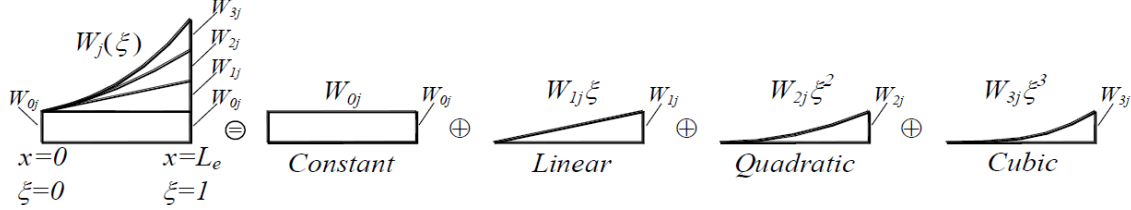

Figure 4: Cubic bending moment diagram decomposition (Bebiano *et al.* 2007)

$$[K^e] = \begin{bmatrix} [K^{11}] & [0] & [0] & [0] & [K^{15}] & \dots \\ & [K^{22}] & [0] & [0] & [K^{25}] & \dots \\ & & [K^{33}] & [0] & [K^{35}] & \dots \\ & & & [K^{44}] & [K^{45}] & \dots \\ & & & & [K^{55}] & \dots \\ sim. & & & & & \ddots \end{bmatrix} \qquad [G^e] = \begin{bmatrix} [0] & [0] & [0] & [0] & [G^{15}] & \dots \\ & [G^{22}] & [0] & [G^{24}] & [G^{25}] & \dots \\ & & [G^{33}] & [G^{34}] & [G^{35}] & \dots \\ & & & [G^{44}] & [G^{45}] & \dots \\ & & & & [G^{55}] & \dots \\ sim. & & & & & \ddots \end{bmatrix} \tag{13}$$

where the superscripts indicate 4x4 sub-matrices associated with pairs of the deformation modes included in the analysis – such components read

$$K_{pr}^{ik} = C_{ik} \int_{Le} \psi_{p,xx} \psi_{r,xx} d\xi + D_{ik} \int_{Le} \psi_{p,x} \psi_{r,x} d\xi + B_{ik} \int_{Le} \psi_p \psi_r d\xi \tag{14}$$

$$G_{pr}^{ik} = W_{ij}^0 X_{ikj} T_{pr}^l - W_{lj}^0 \left(S_{rp}^l X_{jik}^\tau + S_{pr}^l X_{jki}^\tau \right) \tag{15}$$

with

$$T_{pr}^l = \int_{Le} \xi^l \psi_{p,x} \psi_{r,x} d\xi \qquad (l \geq 0) \tag{16}$$

$$S_{pr}^l = \frac{l}{L_e} \int_{Le} \xi^{l-1} \psi_{p,x} \psi_r d\xi \qquad (l \geq 1) \tag{17}$$

where the summation convention applies to subscript l (l=0,1,2,3), indicating the order of the W_{lj} term. The expressions providing the T_{pr}^l and S_{pr}^l components, which incorporate the longitudinal normal stress gradient and shear stress effects, are given explicitly by Bebiano *et al.* (2007). Finally, it is still worth mentioning that, unlike in isolated/individual member GBT buckling analysis, it is indispensable to include deformation mode **1** (axial extension) in GBT frame buckling analyses, in order to ensure joint displacement compatibility – this issue is addressed in next section.

2.3 Member Analysis – Rigid and Semi-Rigid Frames
Before addressing the methodology employed to ensure the displacement compatibility at the frame joints (between non-aligned members), it should be mentioned that the GBT (modal) DOFs are the nodal values and derivatives of the deformation mode amplitude functions, as illustrated in Fig. 5. Moreover, it is also worth noting the designations and meanings of the above DOFs:

6

(i) Axial extension mode (**1**) displacement and its primitive (no physical meaning): $u_a(d_{11})$ and $\int u_a(d_{12})$, for $x=0$, and $u_b(d_{13})$ and $\int u_b(d_{14})$, for $x=L_e$.

(ii) Major/minor-axis bending modes (**2, 3**) transverse displacements and rotations: $v_a(d_{22}+d_{32})$ and $\theta_a(d_{21}+d_{31})$, for $x=0$, and $v_b(d_{24}+d_{34})$ and $\theta_b(d_{23}+d_{33})$, for $x=L_e$.

(iii) Torsion mode (**4**) rotation and its derivative (warping): $\varphi_a(d_{42})$ and $\varphi'_a(d_{41})$, for $x=0$, and $\varphi_b(d_{44})$ and $\varphi'_b(d_{43})$, for $x=L_e$.

(iv) Distortional mode ($k=5,\ldots,5+n_d-1$) amplitudes and their derivatives: $\mu_a(d_{k2})$ and $\mu'_a(d_{kl})$, for $x=0$, and $\mu_b(d_{k4})$ and $\mu'_b(d_{k3})$, for $x=L_e - n_d$ is the number of distortional modes included in the analysis.

(v) Local mode ($k=5+\mathrm{nd},\ldots,n$) amplitudes and their derivatives: $\beta_a(d_{k2})$ and $\beta'_a(d_{kl})$, for $x=0$, and $\beta_b(d_{k4})$ and $\beta'_b(d_{k3})$, for $x=L_e - n$ is the total number of deformation modes included in the analysis.
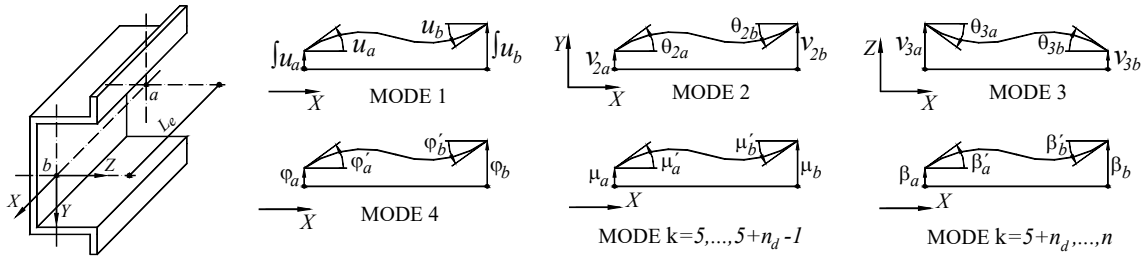

Figure 5: Modal DOF: nodal values and derivatives of the deformation mode amplitude functions

When analyzing frames, a key feature of the methodology employed resides in the fact that member internal nodes and end nodes (joints) must dealt with separately – Figs. 6(a)-(c) illustrate this feature, for the particular case of a portal frame. While in the member internal nodes GBT modal DOFs are always considered (like in isolated members), in the joint nodes (nodes b_r and a_{r+1} in Fig. 6(b)) these same modal DOFs are "transformed" into generalized displacement of the point where the joint is deemed materialized, *i.e.*, "conventional" nodal DOFs. This approach, which makes it much easier (straightforward) to ensure joint displacement compatibility, which was first proposed by Basaglia *et al.* (2008) and amounts to introducing a "joint element concept" – see Fig. 6(c). Essentially, this concept is based on the use of a transformation matrix $[T]$, relating the GBT and nodal DOFs by means of the expressions

$$\{\bar{\xi}\} = [T]\{d\} \Leftrightarrow \begin{Bmatrix} \bar{\xi}_G \\ \bar{\xi}_D \\ \bar{\xi}_L \end{Bmatrix} = \begin{bmatrix} [R_{Y+Z}][R_X][L]_{6x6} & \\ & [I]_{qxq} \end{bmatrix} \begin{Bmatrix} \{d_G\} \\ \{d_D\} \\ \{d_L\} \end{Bmatrix} \tag{18}$$

$$\{\bar{\xi}_G\} = \{U_{\bar{X}} \quad U_{\bar{Y}} \quad U_{\bar{Z}} \quad \Theta_{\bar{X}} \quad \Theta_{\bar{Y}} \quad \Theta_{\bar{Z}} \quad \Theta'_X\}^T \tag{19}$$

$$\{d_G\} = \{u \quad v_Y \quad v_Z \quad \varphi_X \quad \theta_Y \quad \theta_Z \quad \varphi'\}^T \tag{20}$$

$$\{\bar{\xi}_D\} = \{\bar{\mu}'_{k=5} \quad \bar{\mu}_{k=5} \quad \ldots \quad \bar{\mu}'_{k=5+n_d-1} \quad \bar{\mu}_{k=5+n_d-1}\}^T \tag{21}$$

$$\{d_D\} = \{\mu'_{k=5} \quad \mu_{k=5} \quad \ldots \quad \mu'_{k=5+n_d-1} \quad \mu_{k=5+n_d-1}\}^T \tag{22}$$

$$\{\bar{\xi}_L\} = \{\bar{\beta}'_{k=5+n_d} \quad \bar{\beta}_{k=n} \quad \ldots \quad \bar{\beta}'_{k=n} \quad \bar{\beta}_{k=n}\}^T \tag{23}$$

$$\{d_L\} = \{\beta'_{k=5+n_d} \quad \beta_{k=n} \quad \ldots \quad \beta'_{k=n} \quad \beta_{k=n}\}^T \tag{24}$$
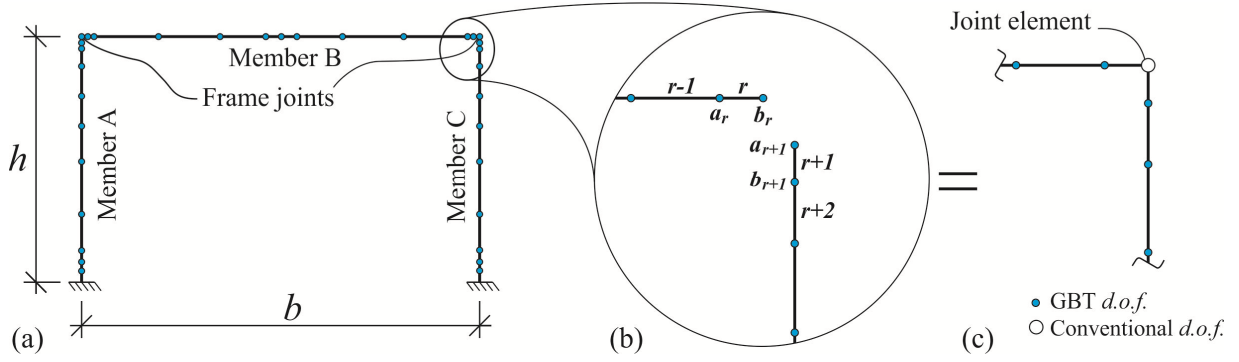
Figure 6: (a) Portal frame discretization into GBT-based beam finite elements, (b) zoomed view of the discretization adopted in a joint vicinity and (c) "joint element" concept

where (i) $\{\bar{\xi}_G\}$ is the sub-vector concerning the global mode nodal generalized displacements (referred to the axes $\bar{X}-\bar{Y}-\bar{Z}$ defined in Fig. 7(a)), (ii) $\{\bar{\xi}_L\}$ and $\{\bar{\xi}_D\}$ are sub-vectors concerning the local and distortional generalized displacements, and (iii) $\{d_G\}$, $\{d_D\}$ and $\{d_L\}$ contain the GBT degrees of freedom, (iv) matrices $[R_{Y+Z}]$ and $[R_X]$, given by

$$[R_{\bar{Y}+\bar{Z}}] = \begin{bmatrix} [R_{\bar{Y}+\bar{Z}}]' & \\ & [R_{\bar{Y}+\bar{Z}}]' \end{bmatrix} \tag{25}$$

$$[R_{\bar{Y}+\bar{Z}}]' = [R_{\bar{Y}}]'[R_{\bar{Z}}]' = \begin{bmatrix} \cos\alpha_{\bar{Y}} & 0 & -\sin\alpha_{\bar{Y}} \\ 0 & 1 & 0 \\ \sin\alpha_{\bar{Y}} & 0 & \cos\alpha_{\bar{Y}} \end{bmatrix} \cdot \begin{bmatrix} \cos\alpha_{\bar{Z}} & -\sin\alpha_{\bar{Z}} & 0 \\ \sin\alpha_{\bar{Z}} & \cos\alpha_{\bar{Z}} & 0 \\ 0 & 0 & 1 \end{bmatrix} \tag{26}$$

$$[R_X] = \begin{bmatrix} [R_X]' & \\ & [R_X]' \end{bmatrix} \tag{27}$$

$$[R_X]' = \begin{bmatrix} 1 & 0 & 0 \\ 0 & \cos\alpha_{\bar{X}} & -\sin\alpha_{\bar{X}} \\ 0 & \sin\alpha_{\bar{X}} & \cos\alpha_{\bar{X}} \end{bmatrix} \tag{28}$$

$$[L] = \begin{bmatrix} 1 & 0 & 0 & 0 & 0 & 0 \\ 0 & 1 & 0 & 0 & 0 & 0 \\ 0 & 0 & 1 & 0 & 0 & 0 \\ 0 & -S_Z & S_Y & 1 & 0 & 0 \\ C_Z & 0 & 0 & 0 & 1 & 0 \\ -C_Y & 0 & 0 & 0 & 0 & 1 \end{bmatrix} \tag{29}$$

describe the rotations associated with the global modes, and (v) $[I]$ is the identity matrix with maximum dimension $q=2m+1$, where m is the number of local and distortional deformation modes included in the analysis. Moreover, $[L]$ is a translation matrix relating the connected element generalized displacements (originally referred to the centroidal or shear centre longitudinal axes, *i.e.*, passing through G and S – see Fig. 7(b)) to parallel reference axes passing through the point/node where the joint is deemed materialized (point $\bar{O}$ in Fig. 7(b). At this point, it is worth mentioning that, since three-dimensional rotation matrices are generally not commutative, it is indispensable to keep the sequence of the operations in order to obtain correct results. According to the coordinate system adopted (see Fig. 7(a)), the transformations are performed in the following sequence: first about the member axis X (Θ_X – see Fig. 7(b)), then about the global axis $\bar{Z}$ ($\Theta_{\bar{Z}}$ – see Fig. 7(a)) and, lastly, about the global axis $\bar{Y}$ ($\Theta_{\bar{Y}}$ – see Fig. 7(b)).
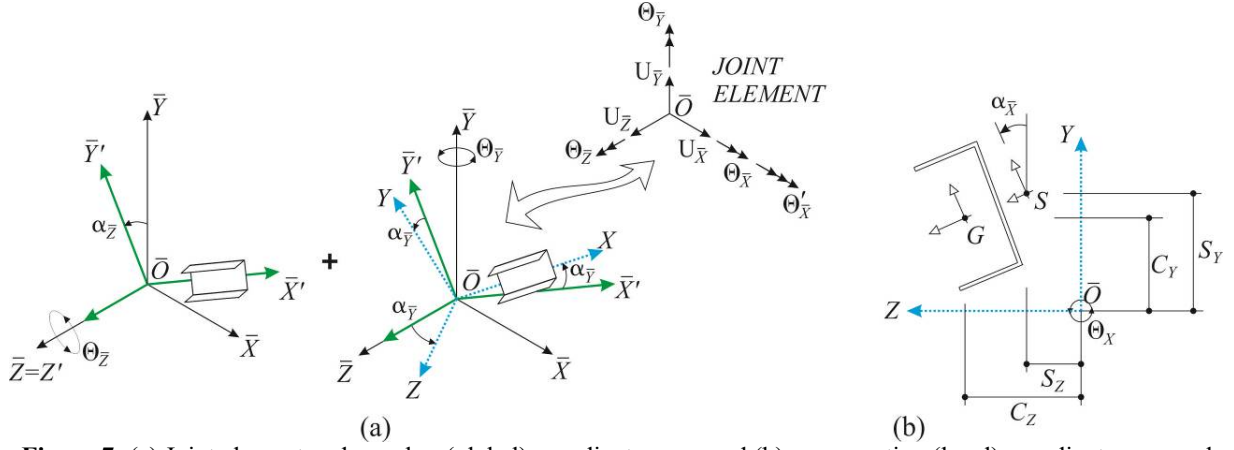
8

Figure 7: (a) Joint element and member (global) coordinate axes, and (b) cross-section (local) coordinate axes and relative positions of points G, S and $\bar{O}$

After using the transformation matrix defined in Eq. (18), one is led to, in the most general case, 7 global DOFs and q-1 DOFs associated with local and distortional modes, which must satisfy

$$\{\bar{\bar{\xi}}_G\}_{b_r} = \begin{bmatrix} [W]_{7x7} & \\ & \Pi \end{bmatrix} \{\bar{\bar{\xi}}_G\}_{a_{r+1}} \tag{30}$$

where (i) subscripts b and a identify the connected member end cross-sections r and $r+1$ (see Fig. 6(b)), (ii) Π are constraint conditions ensuring compatibility between wall warping and flexural displacements (iii) sub-matrix $[W]$, defined by

$$\begin{Bmatrix} U_{\bar{X}} \\ U_{\bar{Y}} \\ U_{\bar{Z}} \\ \Theta_{\bar{X}} \\ \Theta_{\bar{Y}} \\ \Theta_{\bar{Z}} \\ \Theta'_X \end{Bmatrix}_{b_r} = \begin{bmatrix} W_{11} & & & & & & \\ & W_{22} & & & & & \\ & & W_{33} & & & & \\ & & & W_{44} & & & \\ & & & & W_{55} & & \\ & & & & & W_{66} & \\ & & & & & & \Gamma \end{bmatrix} \begin{Bmatrix} U_{\bar{X}} \\ U_{\bar{Y}} \\ U_{\bar{Z}} \\ \Theta_{\bar{X}} \\ \Theta_{\bar{Y}} \\ \Theta_{\bar{Z}} \\ \Theta'_X \end{Bmatrix}_{a_{r+1}} \tag{31}$$

is a diagonal matrix whose components (W_{ii}) relate the generalized global displacements and rotations of each end cross-section. In particular, W_{77} (Γ) is a constant relating the torsional rotation derivatives, *i.e*, quantifying the torsion warping transmission at the joint under consideration – its determination constitutes a non-trivial task, which is briefly in the next sub-section. Furthermore, it is worth noting that the constraint conditions Π must be established for each particular combination of end cross-section shape and joint configuration (no generality is possible). For a joint connecting members with cross-section discretizations involving i natural and j intermediate nodes, such conditions are cast in the form

$$\Pi_{i,i} = \{\Delta\}^T \{\phi_k\} = 0 \tag{32}$$

where the vector $\{\Delta\}$ components are either warping ($u_k(s)$) or wall flexural ($w_k(s)$) functions. Only the particular constraint conditions valid for joints connecting two orthogonal lipped I-section members are addressed in this work. For the joints connecting plain I-section members, the constraint conditions developed by Basaglia (2008) are employed in this work without any modifications.

9

Once all frame support and joint compatibility conditions are enforced, it becomes possible to obtain the frame linear ($[\hat{K}]$) and geometric ($[\hat{G}]$) stiffness matrices, the last step required to establish the sought buckling eigenvalue problem – the "hat" identifies the stiffness matrices already incorporating the joint compatibility conditions. Both the above matrices are associated with "mixed" degrees of freedom: GBT modal and conventional nodal ones. Thus, since the compatibility matrix $[\Omega]$ satisfies the relation

$$\{\hat{\delta}\} = [\Omega]^T \{\delta\} \tag{33}$$

where $\{\hat{\delta}\}$ is a "mixed" vector, combining generalized displacements and GBT degrees of freedom, the buckling eigenvalue problem to be solved can be readily obtained as

$$([\hat{K}] + \lambda[\hat{G}]) = [\Omega]^T ([K] + \lambda[G])[\Omega] \tag{34}$$

Naturally, after solving the buckling eigenvalue problem, the nodal degrees of freedom are "transformed back" into GBT ones, thus obtaining a fully modal solution.

2.3.1 Joint compatibility conditions – global modes and torsion warping transmission
The compatibility between the connected member end cross-section generalized global displacements and rotations is enforced by means of a particular set of relations specifically established for a given joint configuration, *i.e.*, the matrix diagonal components W_{ii} appearing in Eq. (31). Their values depend on the characteristics of the joint, such as the presence of localized supports, stiffening plates, bolts or weld fillets. Particular attention must be devoted to the determination of the component W_{77} (constant Γ), which deals with the warping transmission associated with torsion.

Although the quantification of the torsion warping transmission at arbitrary joints constitutes a major obstacle to the assessment of the global spatial behavior of thin-walled frames by means of beam finite elements, recent investigations have shed new light on this matter. In particular, Basaglia *et al.* (2008) proposed kinematical models to quantify the torsion warping transmission (i) in three joint configurations (diagonal-stiffened, box-stiffened and diagonal/box-stiffened) connecting two or more non-aligned plain channel and I-section members with web continuity and (ii) in unstiffened joints connecting two members whose flanges lie in the same plane (flange continuity). A bit later, the same authors (Basaglia *et al.* 2009) proposed similar models for lipped channel and I-section members – the latter is used in this work. An alternative approach was very recently followed by Shayan & Rasmussen (2014), who developed a joint model, intended to be used together with beam finite elements, that combines a sub-structuring technique with the inclusion of linear springs. Because this model incorporates 3D shell finite element modeling of some joint components, it provides a more accurate and general simulation of the joint behavior.

Since this work deals exclusively with GBT buckling analysis, the approach adopted to handle the torsion warping transmission is the use of the kinematic models developed by Basaglia *et al.* (2009), which were numerically validated by means of shell finite element simulations. In particular, it was shown by these authors that the joints exhibiting flange continuity (see Fig. 8(a)) are associated with a complete and direct torsion warping transmission, which corresponds to inserting *Γ=1* in Eq. (31). However, in unstiffened joints with web continuity (see Fig. 8(b)), it is commonly accepted (Sharman 1985, Morrell *et al.* 1996, Basaglia *et al.* 2009) that the torsion warping transmission is incomplete, because there is strain energy absorption through joint local/web deformation (wall transverse bending) – therefore, the value of *Γ* to be included in Eq. (31) is in the range *0≤Γ<1*. Indeed, in such joints full compatibility between the warping and in-plane displacements of the connected end cross-sections must be enforced, which precludes the *a priori* torsion warping transmission quantification – such quantification requires a compatibility analysis.
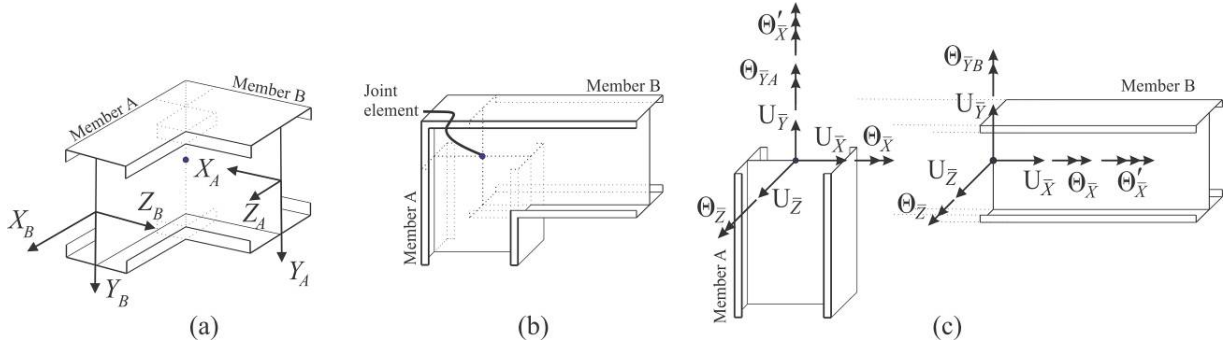
Figure 8: Joints connecting lipped I-section members with (a) web and (b) flange continuity

In web continuity joints connecting two orthogonal members (see Fig. 6(a)), (i) the warping displacements of one end cross-section must be fully compatible with the in-plane (flexural) displacements of the other (*i.e.*, there is a null torsion warping transmission) and (ii) the torsional rotation of one member causes a combination of local deformation, bending and torsion of the other member. This means that assessing the relation between the torsional rotation of one member end cross-section and the bending rotation of the other (*e.g.*, the rotations $\Theta_{\bar{Y}A}$ and $\Theta_{\bar{Y}B}$ of members A and B, in Fig. 8(b)) is only possible by resorting to shell finite element analysis – Basaglia *et al.* (2009) proposed a set of constraint equations that can be used to obtain a fairly good quantification of this relation (they are addressed in Section 2.3.2).

Following the approach of Basaglia *et al.* (2008), a direct complete relation between the generalized rotations and displacements caused by axial extension and bending is adopted in this work. However, particular attention is paid to the end cross-section DOFs concerning major-axis flexural rotation $\Theta_{\bar{Z}}$ (see Fig. 8(c)), *i.e.*, those associated with the joint semi-rigidity considered. Indeed, in order to characterize the joint semi-rigidity adequately, by means of springs, the equation relating the major-axis flexural rotations has to be removed from Eq. (31), which amounts to treating them independent – this issue is addressed in Section 2.3.3. Thus, the end cross-section global displacements and rotations satisfy the conditions

$$
\begin{Bmatrix} U_{\bar{X}} \\ U_{\bar{Y}} \\ U_{\bar{Z}} \\ \Theta_{\bar{X}} \\ \Theta_{\bar{Y}} \\ \Theta'_X \end{Bmatrix}_{b_r} =
\begin{bmatrix} 1 & & & & & \\ & 1 & & & & \\ & & 1 & & & \\ & & & W_{44} & & \\ & & & & W_{55} & \\ & & & & & \Gamma \end{bmatrix}
\begin{Bmatrix} U_{\bar{X}} \\ U_{\bar{Y}} \\ U_{\bar{Z}} \\ \Theta_{\bar{X}} \\ \Theta_{\bar{Y}} \\ \Theta'_X \end{Bmatrix}_{a_{r+1}}
\tag{35}
$$

where it should be noted that (i) the torsion warping transmission is always null (web continuity joints connecting two orthogonal members) and (ii) components W_{44} and W_{55} are obtained from the specific constraint equations addressed in Section 2.3.2.

2.3.2 Constraint conditions – web continuity
Consider the portal frame depicted in Fig. 6(a), built from identical orthogonal lipped I-section members connected with web continuity (see Fig. 8(b)). The displacement/rotation compatibility conditions at the flanges, web and lips of the connected member end cross-sections correspond to the satisfaction of the constraint equations Π, generally defined in Eq. (32) and whose inclusion in the frame buckling analysis is addressed below:[1]

---

[1] A more detailed account of the establishment of these constraint conditions can be found in the work of Basaglia *et al.* (2009).

(i) *Flange compatibility.* As shown in Fig. 9(a), point J identifies the assumed connection location (intersection of the two member centroidal/shear centre axes). Since the angle between the member centroidal axes (α) is non-null, it is necessary to consider additional axes (Q-Q), located at the intersection of the flanges (distance f from the end cross-sections – see Fig. 9(a)). The compatibility of the flange displacements/rotations is associated with imposing the equality between (i$_1$) the transverse bending displacements of one member end cross-section and the warping displacements (due to torsion and/or distortion) of the other, and (i$_2$) the transverse bending rotations of the two members. Therefore, it is necessary to impose twelve constraint equations Π_Q, concerning the points corresponding to the inner (Q'_{iA} vs. Q''_{iB} and Q'_{iA} vs. Q''_{iB}) and outer (Q'_{eA} vs. Q''_{eB} and Q'_{eA} vs. Q''_{eB}) flange-lip intersections – note that only the former correspond to points of the GBT model (the latter are absent from this model). They read

$$\Pi_{Q_{pA}}^I = \sin\alpha \left[u_4(Q_{pA})\phi_{4,x}\left(x_{Q_{pA}}\right) + \sum_{k=5}^{5+n_d-1} u_k(Q_{pB})\,\phi_{k,x}\left(x_{Q_{pB}}\right) \right] - \sum_{k=5}^{n} w_k(Q_{pB})\,\phi_k\left(x_{Q_{pB}}\right) = 0 \tag{36}$$

$$\Pi_{Q_{pB}}^{II} = \sin\alpha \left[u_4(Q_{pB})\phi_{4,x}\left(x_{Q_{pB}}\right) + \sum_{k=5}^{5+n_d-1} u_k(Q_{pB})\,\phi_{k,x}\left(x_{Q_{pB}}\right) \right] - \sum_{k=5}^{n} w_k(Q_{pA})\,\phi_k\left(x_{Q_{pA}}\right) = 0 \tag{37}$$

$$\Pi_{Q_p}^{III} = \sum_{k=5}^{n} w_k(Q_i)\,\phi_{k,x}(x_{Q_i}) - \sum_{k=5}^{n} w_k(Q_i)\,\phi_{k,x}(x_{Q_i}) = 0 \tag{38}$$

where (i$_1$) subscript p is either i or e, (i$_2$) Q stands for Q' or Q'' and, according to Fig. 9(b), (i$_3$) $f=h/2\,tan(\alpha/2)$ and $x_{Q_i}=L{-}f$.

(ii) *Web compatibility.* Concerns the equality between the transverse bending displacements and rotations at the web points depicted in Fig. 9(c), R' to R''' – the number of such points considered (three in this case), depends on the level of approximation required. For each web point, two constraint equations Π_R must be imposed, namely

$$\Pi_R^I = \sum_{k=5}^{n} w_k(R_A)\,\phi_k(x_{R_A}) - \sum_{k=5}^{n} w_k(R_B)\,\phi_k(x_{R_B}) = 0 \tag{39}$$

$$\Pi_R^{II} = \sum_{k=5}^{n} w_k(R_A)\,\phi_{k,x}(x_{R_A}) - \sum_{k=5}^{n} w_k(R_B)\,\phi_{k,x}(x_{R_B}) = 0 \tag{40}$$

(iii) *Lip compatibility.* Similarly to the web, it concerns the equality between the transverse bending displacements and rotations at points corresponding to the intersections of the lip free ends – points T_{eA} vs. T_{eB} and T_{iA} vs. T_{iB} in Fig. 9(d). Four constraint equations Π_T must be imposed, namely

$$\Pi_T^I = \sum_{k=5}^{n} w_k(T_{pA})\,\phi_k\left(x_{T_{pA}}\right) - \sum_{k=5}^{n} w_k(T_{pB})\,\phi_k\left(x_{T_{pB}}\right) = 0 \tag{41}$$

$$\Pi_T^{II} = \sum_{k=5}^{n} w_k(T_{pA})\,\phi_{k,x}\left(x_{T_{pA}}\right) - \sum_{k=5}^{n} w_k(T_{pB})\,\phi_{k,x}\left(x_{T_{pB}}\right) = 0 \tag{42}$$

where (iii$_1$) subscript p is either i or e, and (iii$_2$) T stands for T' or T''.
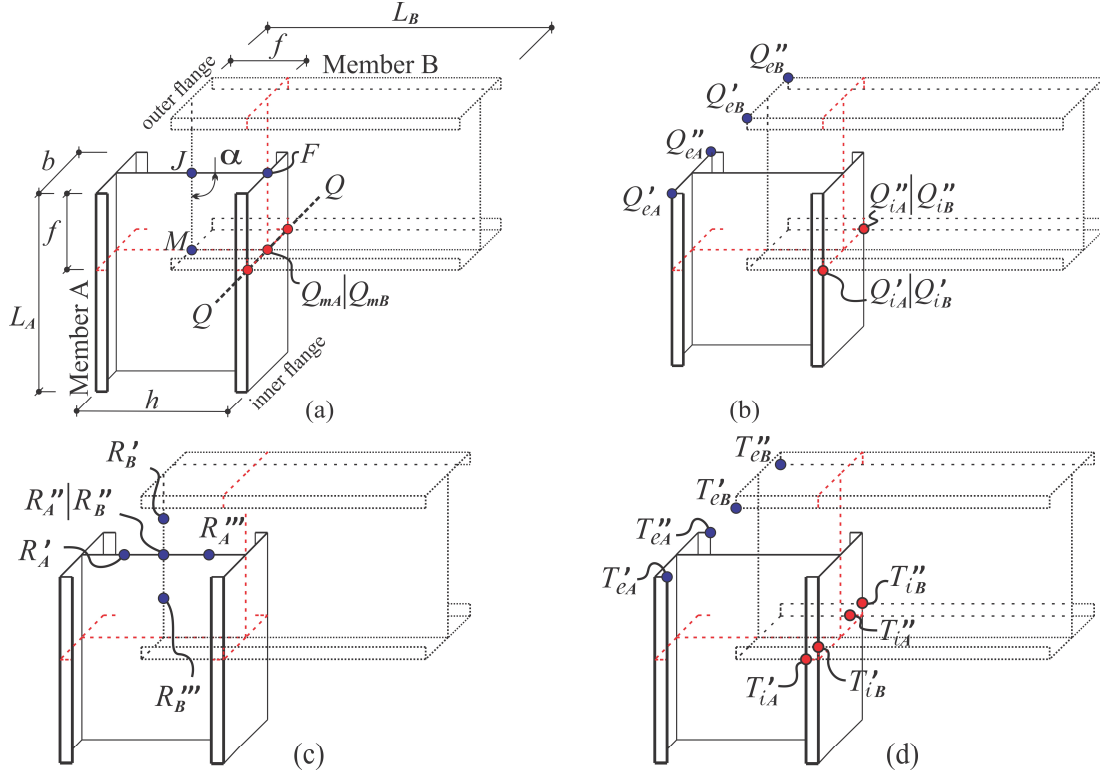
Figure 9: Unstiffened joint connecting two orthogonal lipped I-section members with web continuity: (a) overall configuration and (b) flange, (c) web and (d) lip nodes to be constrained

Furthermore, the joint compatibility of the global rotations stemming from lateral (global) bending and/or torsion, addressed in Section 2.3.1, must also be ensured by means of constraint equations − they are not covered by Eq. (27). For the case of orthogonal plain channel and I-section members connected with web continuity, Basaglia *et al.* (2009) proposed the consideration of two additional sets of constraint equations, Ψ_T and Ψ_Θ. The first one (Ψ_T) concerns the equality between the transverse displacement stemming from lateral bending and/or torsional rotation at the intersection of the connected member inner flange-web longitudinal edges (point $Q_{mA}|Q_{mB}$ in Fig. 9(a)). Similarly, the second set (Ψ_Θ) corresponds to constraint conditions involving the lateral bending rotations at points F, J and M (see Fig. 9(a)). It is assumed in this work that the above constraint equations remain valid for lipped I-section members connected with web continuity − they read

$$\Psi_T^I = \sum_{k=3}^{4} w_k(Q_{mA})\,\phi_k\!\left(x_{Q_{mA}}\right) - \sum_{k=3}^{4} w_k(Q_{mB})\,\phi_k\!\left(x_{Q_{mB}}\right) = 0 \tag{43}$$

$$\Psi_\Theta^I = \frac{w_3(M_A)\phi_{k,x}\!\left(x_{M_A}\right)}{w_3(J)\phi_{k,x}\!\left(x_J\right)} = \frac{1}{0.75}$$

$$\Psi_\Theta^{II} = \frac{w_3(F_B)\phi_{k,x}\!\left(x_{F_B}\right)}{w_3(J)\phi_{k,x}\!\left(x_J\right)} = \frac{1}{0.75} \tag{44}$$

where (i) Q_{mA} and Q_{mB} stand for the intersection point of the connected inner flange-web longitudinal edges, (ii) M_A belongs to member A and (iii) F_B belongs to member B, as illustrated in Fig. 9(a).

13

2.3.3 Semi-rigid joints – spring finite element and compatibility conditions

Linear springs were first included in the GBT adjacent equilibrium equation system by Camotim *et al.* (2008), with the objective of simulating elastic supports or partial bracing arrangements in the context of the buckling analysis of isolated members – naturally, such linear springs connected member points to locations external to the member. A similar approach is employed in this work to simulate the joint semi-rigidity – the difference resides in the fact that, now, the linear springs connect two member points. The most convenient implementation consists of considering zero-length finite elements, such as that depicted in Fig. 10, connecting members r and $r+1$ through the respective end nodes b_r and a_{r+1}. This finite element consists of two linear springs, associated with translational (k_{jd}) and rotational ($k_{j\theta}$) DOFs, and involves each of the j GBT deformation modes included in the analysis and exhibiting non-null values of those translation and rotation. The equilibrium of the spring element, located at a given cross-section and associated with an arbitrary deformation mode j, corresponds to the equation system

$$[k]_j \{\Delta_j\}^T \{\phi_j\} = \{F_j\} \tag{45}$$

where $[k]_j$ is the spring element stiffness matrix, relating the generalized force (F_j) and displacement (Δ_j) vectors associated with the linear spring action on the deformation mode under consideration. In matrix form, Eq. (45) can be rewritten as

$$\begin{bmatrix} k_{j\theta} & 0 & -k_{j\theta} & 0 \\ 0 & k_{jd} & 0 & -k_{jd} \\ -k_{j\theta} & 0 & k_{j\theta} & 0 \\ 0 & -k_{jd} & 0 & k_{jd} \end{bmatrix} \begin{Bmatrix} \Delta_{j,x}(b_r) \\ \Delta_j(b_r) \\ \Delta_{j,x}(a_{r+1}) \\ \Delta_j(a_{r+1}) \end{Bmatrix} \begin{Bmatrix} \phi_{j,x}(b_r) \\ \phi_j(b_r) \\ \phi_{j,x}(a_{r+1}) \\ \phi_j(a_{r+1}) \end{Bmatrix} = \begin{Bmatrix} F_{j,x}(b_r) \\ F_j(b_r) \\ F_{j,x}(a_{r+1}) \\ F_j(a_{r+1}) \end{Bmatrix} \tag{46}$$

where (i) k_{jd} and $k_{j\theta}$ are the translational and rotational spring stiffness values, (ii) Δ_j and $\Delta_{j,x}$ are the values and derivatives of the generalized displacements associated with deformation mode j ($u_j(s)$, $v_j(s)$, $w_j(s)$ and/or their derivatives with respect to s) occurring before (b_r) and after (a_{r+1}) the cross section (global modes) or cross-section point (distortional or local modes) where the spring is located, (ii) ϕ_j and $\phi_{j,x}$ are the value and derivative of the amplitude of deformation mode j before and after that cross-section and (iii) F_j and $F_{j,x}$ are the generalized forces before and after the cross section under consideration. It is worth noting that the springs considered in this work involve exclusively flexural rotations associated with major-axis bending ($j=2$).

Finally, including the spring elements into the GBT frame (discretized) adjacent equilibrium equation system is straightforward: since the DOFs of these element stiffness matrices, which are of dimension *4n* (*n* is the number of deformation modes involved) coincide with the GBT ones, the assembly with the member element stiffness matrices can be routinely performed by means of standard techniques, to obtain the adjacent equilibrium equation (Eq. (34)), which defines the frame buckling eigenvalue problem.
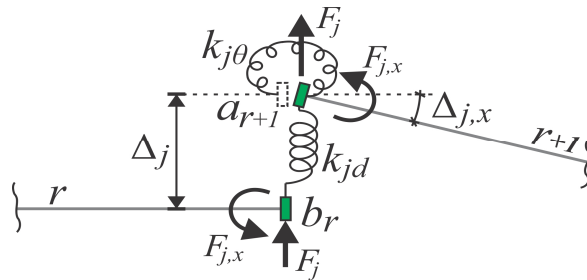

Figure 10: Schematic representation of a GBT zero-length spring element relating connected node translations and rotations

3. Validation and Illustrative Examples

In order to validate the formulation and numerical implementation developed, and also to illustrate its capabilities and potential, this section presents and discusses results concerning the buckling behavior of two simple plane portal and L-shaped frames with semi-rigid joints associated with (in-plane) major-axis flexural rotations. The geometries of the frames analyzed were selected in order to ensure that critical buckling may occur in modes exhibiting different natures, namely global, distortional and local critical buckling modes. All the frame joints are unstiffened, exhibit web continuity and are fully braced against out-of-plane flexural displacements – torsional rotations are possible. Several GBT buckling results are compared with values obtained from beam or shell finite element analyses performed in the code ANSYS (SAS 2009) – in the latter case, it is necessary to resort to a kind of "artificial modeling".

The kinematic relations presented in Sections 2.3.1 and 2.3.2, for unstiffened joints with web continuity (see Fig. 8(b)), are adopted to model the torsion warping transmission and in-plane flexural displacement compatibility at the frame joints. The stiffness of the spring simulating the joint major-axis flexural semi-rigidity influences the frame buckling behavior in two different ways: (i) by changing the bending moment (mostly) and axial force diagrams acting on the frame members and/or (ii) by altering the frame susceptibility to in-plane global/flexural buckling. At this stage, it is worth noting that relating the stiffness values adopted to more or less realistic frame joint configurations is beyond the scope of this work. However, this is a very important issue that will be addressed in the next step of this investigation[2].

3.1 Portal Frames Formed by Lipped I-Section Members

Consider the portal frames depicted in Figs. 11(a)-(b), whose columns and beam are made of steel (Young's modulus E=210GPa and Poisson's ratio ν=0.3), exhibit the lipped I-section displayed in Fig. 3(a) and have lengths L_c=410cm and L_b=510cm, respectively. The two frames differ only in the loading: vertical forces P applied at joints B and C (columns under compression) or lateral forces applied at the left column (P) and beam ($0.8P$) mid-span cross-section shear centers (columns and beams under axial force and major-axis bending). The frames have fixed column bases and semi-rigid joints with equal rotational stiffness k (recall that both joints are fully restrained against out-of-plane flexural displacements).

The first set of analyses, aimed at obtaining an initial (trivial) validation of the formulation, concerns the frame of Fig. 11(a) and includes only modes **1** and **2**: axial extension and major-axis (in-plane) flexure. Fig. 12(a) shows the variation of the semi-rigid frame critical buckling load $P_{cr.k}$, normalized with respect
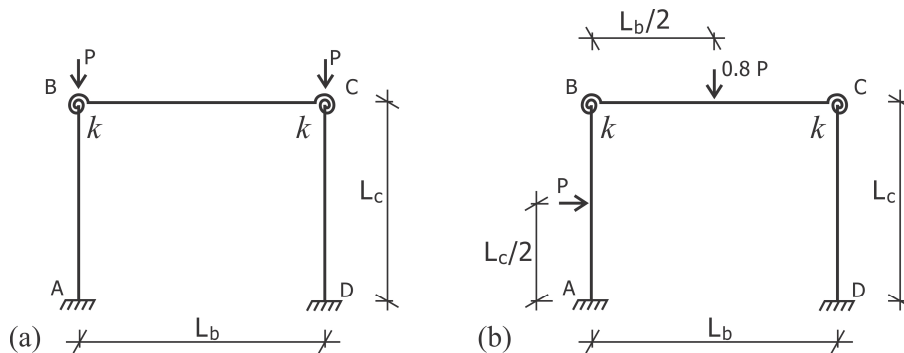

Figure 11: Portal frames with semi-rigid joints under (a) two vertical loads applied at the joints, and (b) transverse loads applied at the left column and beam mid-span cross-sections

---

[2] It is well known that the mechanical characteristics of each component of a particular joint, connecting frame members, contribute differently to its overall flexural stiffness. The determination of such stiffness constitutes a rather complex task that may be done, for instance, using the so-called "Component Method" prescribed in Eurocode 3 – Part 1-8 (CEN 2005).
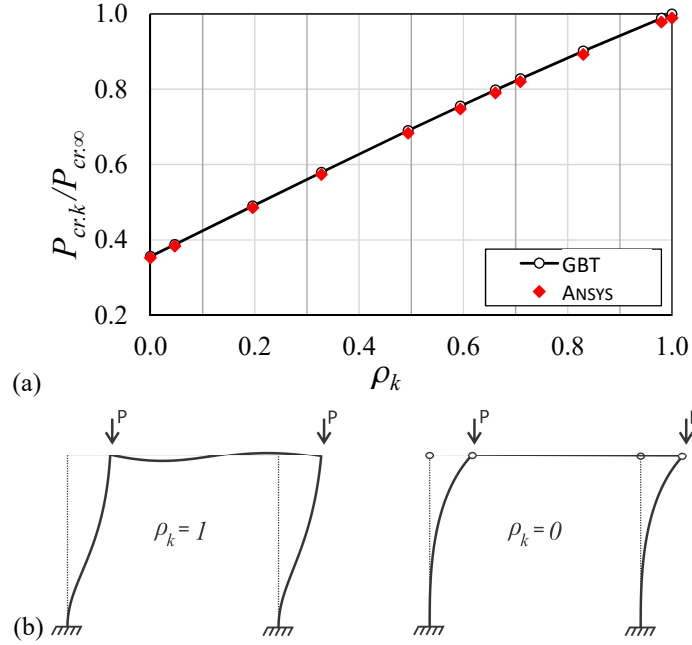
Figure 12: Portal frame: (a) variation of $P_{cr.k}/P_{cr.\infty}$ with ρ_k and (b) critical buckling shapes for $\rho_k=1$ and $\rho_k=0$

to the rigid frame value ($P_{cr.\infty}=\pi^2EI/1.423L_c^2$, where I is the column and beam in-plane moment of inertia − see, for instance, Chajes 1974), against a fixity factor $\rho_k=1/(1+3EI/kL_b)$, dependent on the joint stiffness k and introduced by Monforton & Wu (1963) − note that a rigid and pinned connection correspond to $\rho_k=1$ and $\rho_k=0$, respectively, and semi-rigid connections have ρ_k values comprised between 0 and 1[3]. After observing the results displayed in Fig 12(a), the following remarks are appropriate:

(i) As expected, the critical buckling loads and mode shapes provided by the GBT and ANSYS (beam finite elements with linear rotational springs) analyses virtually coincide. Fig. 12(b) shows the critical buckling modes shapes of the frames with rigid ($\rho_k=1$) and pinned ($\rho_k=0$) joints − those concerning frames with semi-rigid joints fall in between these two.

(ii) There is an almost linear relationship between $P_{cr.k}$ and ρ_k. Moreover, for this particular case, the frame critical buckling load increases by about 185% as ρ_k varies between 0 and 1.

(iii) Despite the inherent simplicity of this illustrative example, it just confirms that the linear springs are correctly incorporated in the GBT buckling analysis (with only two deformation modes included).

The second set of analyses involve the frame of Fig. 11(b), whose members experience combinations of axial compression and major-axis bending. In this case, a key aspect concerning the influence of the joint semi-rigidity, which will be addressed next, is the variation of the member bending moment diagrams, illustrated in Fig. 13(a), showing those diagrams for the frames with rigid ($\rho_k=1$) and pinned ($\rho_k=0$) joints, respectively − naturally, the diagrams corresponding to other ρ_k values lie in between these two.

The GBT buckling analyses of these frames included the first 10 deformation modes depicted in Fig. 3(c) and involved column and beam longitudinal discretizations into 11 and 12 beam finite elements, respectively. On the other hand, the ANSYS shell finite element analyses of the semi-rigid frames were performed in an "artificial" manner: because the frame instability is triggered far from the joint regions, it

---

[3] For the frame with pinned joints, one has $P_{cr.0}=\pi^2EI/4L_c^2$, since the frame behaves like two independent pinned-fixed columns with sway displacements allowed.
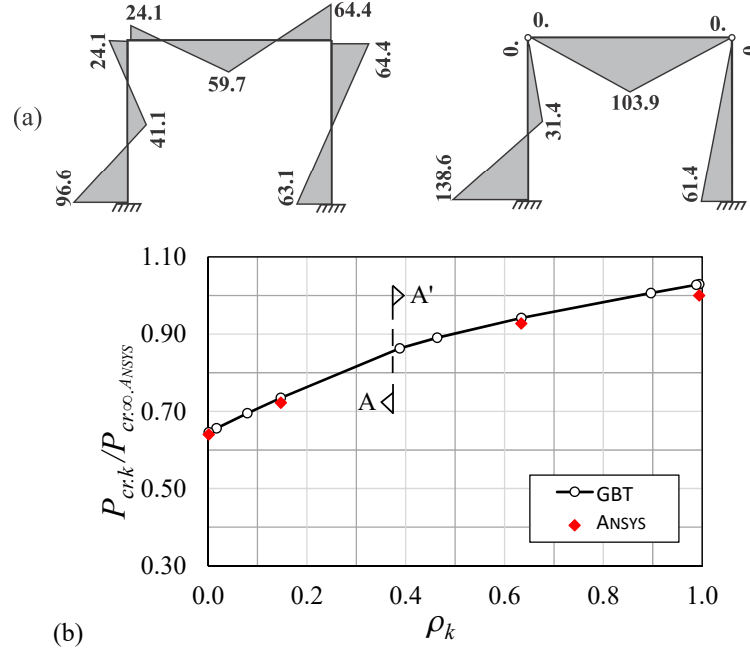
Figure 13: (i) Bending moment diagrams (kN.cm) of frames with for $\rho_k=1$ and $\rho_k=0$, and (b) variation of $P_{cr.k}/P_{cr.\infty}$ with ρ_k

is assumed that its columns and beam may be analyzed separately/individually, (i) subjected to the axial force and bending moment diagrams obtained from the semi-rigid frame pre-buckling analysis and (ii) with simple end supports (allowing for torsional rotations)[4].

Table 1 shows the critical buckling loads obtained from the GBT ($P_{cr.k.GBT}$) and ANSYS ($P_{cr.k.ANSYS}$) analyses for various ρ_k values as well as the ratio between them ($\Delta_{cr.k}=P_{cr.k.GBT}/P_{cr.k.ANSYS}$) and the nature of the associated buckling modes. In addition, the values of the normalized joint stiffness, kL_b/EI, are also given. Furthermore, Fig. 13(b) plots the variation of the semi-rigid frame critical buckling load $P_{cr.k}$, normalized with respect to $P_{cr.\infty ANSYS}$, with the fixity factor ρ_k, and Figs. 14(a)-(d) to 16(a)-(d) show the ANSYS and GBT critical buckling mode shapes of the frames with pinned ($\rho_k=0$), rigid ($\rho_k=1$) and semi-rigid ($\rho_k=0.39$) joints, respectively. Each figure shows (i) overall views of the frame critical buckling mode provided by

Table 1: Buckling results concerning the frame of Fig. 11(b) (loads in kN)

ρ_k	k_rL_b/EI	$P_{cr.k.GBT}$	$P_{cr.k.ANSYS}$	Mode nature	$\Delta_{cr.k}(\%)$
1.00	520	178.5	173.4	D (left column)	1.03
0.99	260	178.2	-	D (left column)	-
0.90	26	174.5	-	D (left column)	-
0.63	5.0	163.3	160.8	D (left column)	1.02
0.46	2.5	154.4	-	D (left column)	-
0.39	1.9	149.6	-	D (left column)	-
0.15	0.5	127.4	125.2	F-T-D (beam)	1.02
0.08	0.3	120.5	-	F-T-D (beam)	-
0.02	0.1	113.8	-	F-T-D (beam)	-
0.00	0.0	112.1	110.9	F-T-D (beam)	1.01

---

[4] The need to adopt this approach is due to the fact that it was not possible to incorporate the linear springs concerning only major-axis flexure (GBT deformation mode **2**) in the shell finite element model. In the future, it is intended to model the "real joint" in the ANSYS analyses and to compare the results obtained with those provided by GBT with the linear spring stiffness values determined, using the "Component Method" (CEN 2005), on the basis of the above "real joint" configuration.
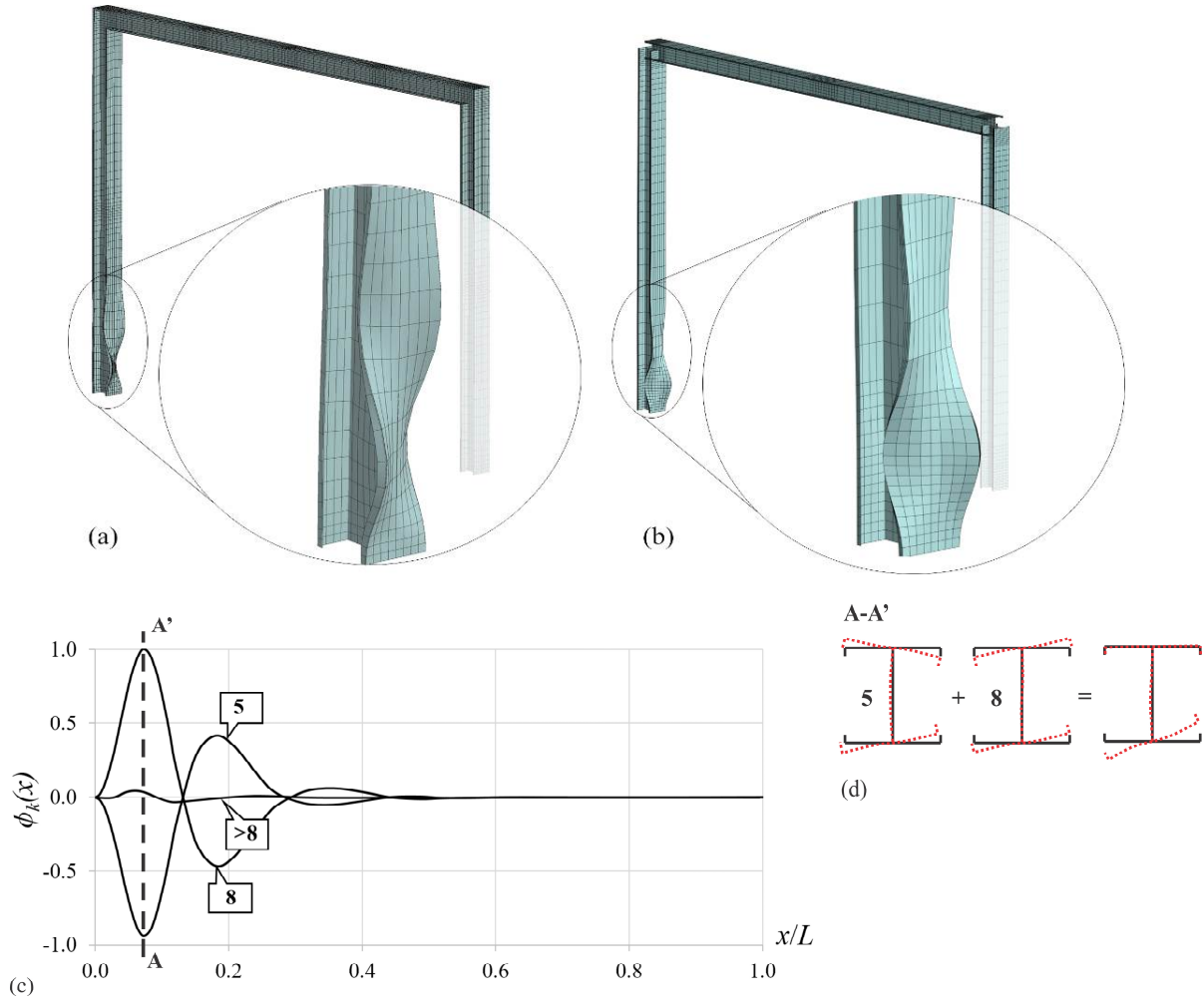
Figure 14: Portal frame with pinned joints: (a) ANSYS and (b) GBT views of the critical buckling mode shape, (c) GBT modal amplitude functions of the left column, at buckling, and (d) corresponding most deformed cross-section modal decomposition

the ANSYS[5] and GBT[6] analyses (including blow-ups of the buckled region), (ii) the GBT deformation mode amplitude functions, concerning the frame critical buckling mode, of the member triggering the frame instability, and (iii) a GBT modal decomposition of the most deformed cross-section of that member (identified by a dashed line in the plot providing the amplitude functions). The observation and analysis of the buckling results presented in Table 1 and Figures 13 to 16 prompt the following remarks:

(i)   Once again, there is a virtual coincidence between the critical buckling loads provided by the GBT (beam finite element) and ANSYS (shell finite element) analyses[7] – the difference never exceeds 3% (the $P_{cr.k.GBT}$ values are always higher). In addition, there is also a remarkable similarity between the three pairs of GBT and ANSYS critical buckling mode representations (see Figs. 14(c)-16(c)) – but the GBT modal amplitude functions provide additional in-depth insight on the buckling mechanics.

_____

[5]   In view of what was mentioned in the previous footnote, the ANSYS view of the frame with semi-rigid joints includes only the member triggering the frame instability – the left column, in this particular case.

[6]   Note that the GBT views are three-dimensional representation of buckling results obtained with beam finite elements, *i.e.*, a finite elements based on a one-dimensional theory.

[7]   Recall that, in the frames with semi-rigid joints, the ANSYS analysis concerns only the member triggering the frame instability – see Fig. 16(a), dealing with the frame with ρ_k=0.39, which shows the critical buckling mode shape of the left column alone.
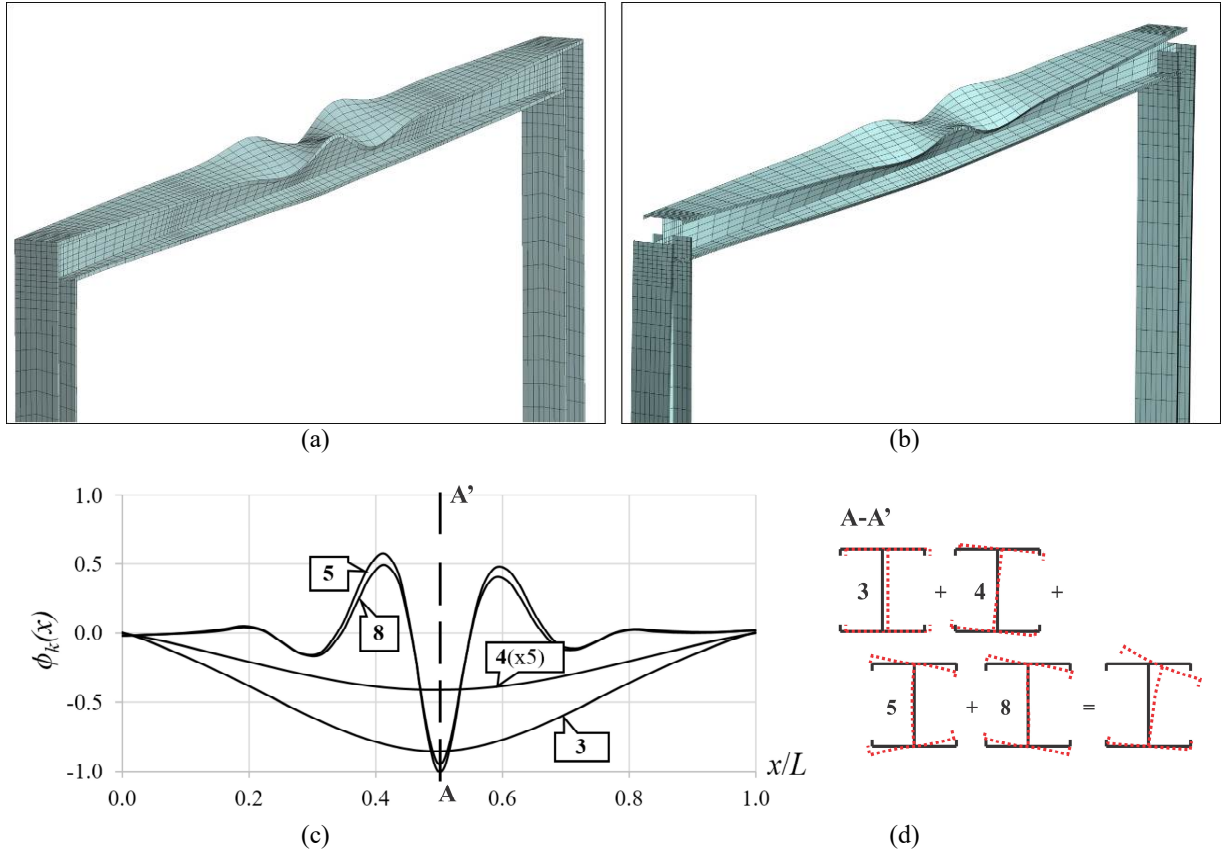
Figure 15: Portal frame with pinned joints: (a) ANSYS and (b) GBT views of the critical buckling mode shape, (c) GBT modal amplitude functions of the beam, at buckling, and (d) corresponding most deformed cross-section modal decomposition

(ii) The rigid and pinned frames exhibit critical distortional (D) and flexural/lateral-torsional-distortional (F-T-D) buckling modes, respectively – the former triggered by the left column (base region) and the latter by the beam (mid-span region). In GBT terms, the buckling of the pinned and rigid frames is governed by (i) the distortional deformation modes **5** and **8** and (ii) the minor-axis flexural (**3**), torsional (**4**) and distortional (**5** and **8**) modes – see Figs. 3(c), 14(c)-(d) and 15(c)-(d). As for the semi-rigid frame whose buckling results are depicted in Fig. 16 (ρ_k=0.39), its critical buckling mode combines deformations in the left column and beam – see Figs. 16(b)-(c).

(iii) The variation of the joint stiffness has a very significant impact on the member bending moment diagrams (see Figure 13(a)) and, in particular, changes the member triggering the frame instability – for instance, while the buckling of the rigid frame is governed by the left column, the instability of the pinned frame is triggered by the beam. In the particular case of the semi-rigid frame shown in Fig. 16 (ρ_k=0.39), the instability is triggered by the left column base region (like in the rigid frame).

(iv) Since the critical buckling modes of the pinned and rigid frames are distortional (left column base region) and lateral-torsional-distortional (beam mid-span region), it is just logical to expect a change in critical buckling mode nature to occur for an intermediate joint stiffness value (*i.e.*, ρ_k value). Indeed, this is the case and the value under consideration is identified in Fig. 13(b) by the dashed line A-A': it corresponds to ρ_k=0.39 (note that the semi-rigid frame with ρ_k=0.15 buckles in a F-T-D mode triggered by the beam).

(v) Fig. 13(b) shows that the relationship between $P_{cr.k}$ and ρ_k is approximately bi-linear – the transition between the two linear segments corresponds to the change in buckling mode nature (ρ_k=0.39). The
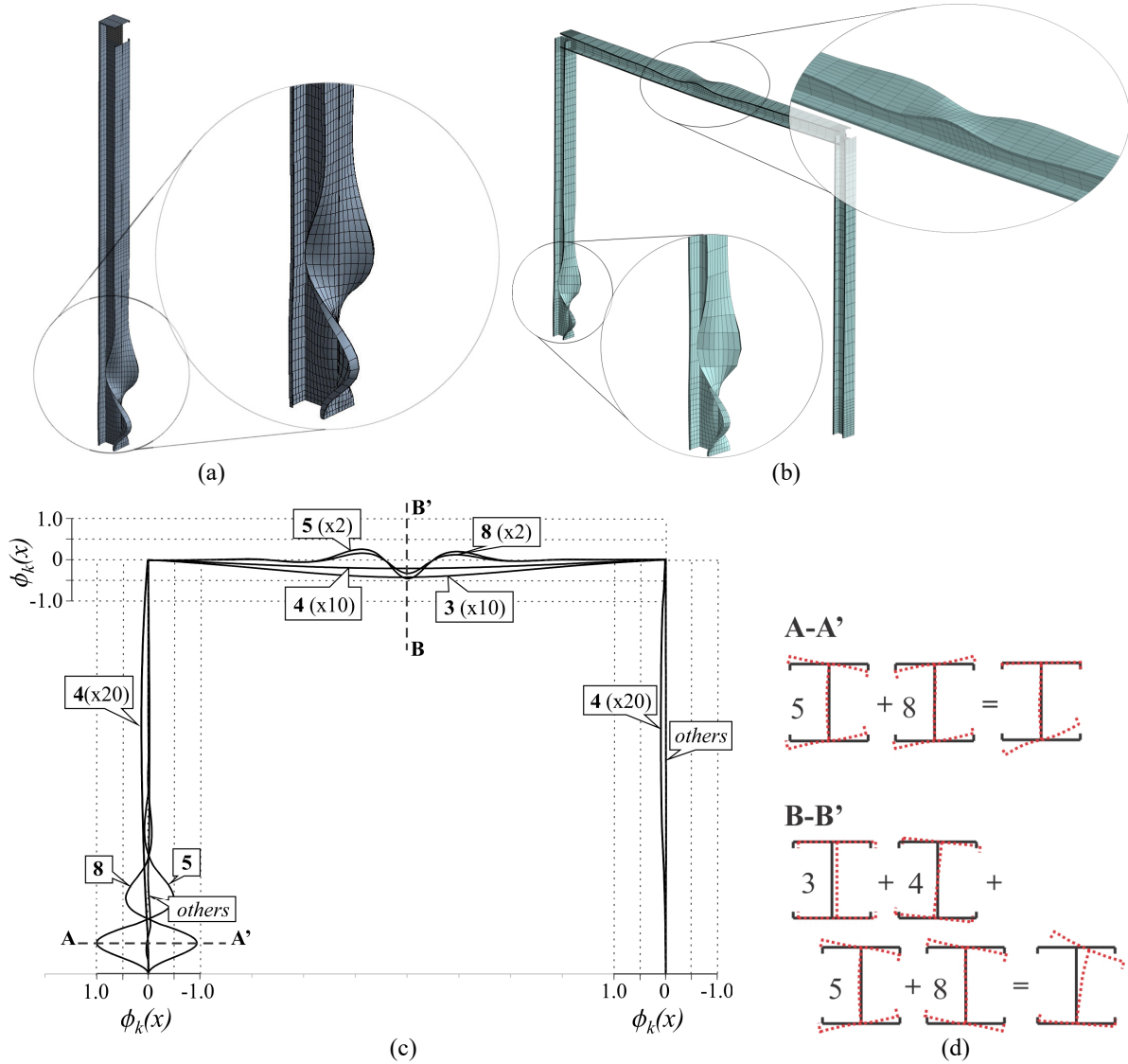
19

Figure 16: Semi-rigid portal frame (ρ_k=0.39): (a) ANSYS and (b) GBT views of the critical buckling mode shape, (c) GBT modal amplitude functions of the frame, at buckling, and (d) corresponding most deformed cross-section modal decompositions

slope of the first segment is moderately higher than that of the second segment, which means that the joint stiffness affects the left column buckling behavior the most.

(vi) For most of the joint semi-rigidity range, the frame critical buckling mode shape exibits deformations exclusively in the left column (higher ρ_k values) or the beam (lower ρ_k values). However, for frames with ρ_k close to the transition between the two above situations ($\rho_k \approx 0.39$), the critical buckling mode involves deformations in both the left column and beam. For instance, the ρ_k=0.39 frame critical buckling mode (see Fig. 16(b)) involves dominant in the left column, but also clearly visible ones in the beam (the right column remains practically undeformed).

3.2 L-shaped Frames Formed by Plain I-Section Members

Consider the L-shaped frame depicted in Fig. 17(a), whose column and beam are made of steel (Young's modulus E=210 GPa and Poisson's ratio v=0.3), exhibit the plain I-section displayed in Fig. 3(a) (with the lips removed) and have lengths L_c=370 cm and L_b=310 cm, respectively. The column base is fixed, the
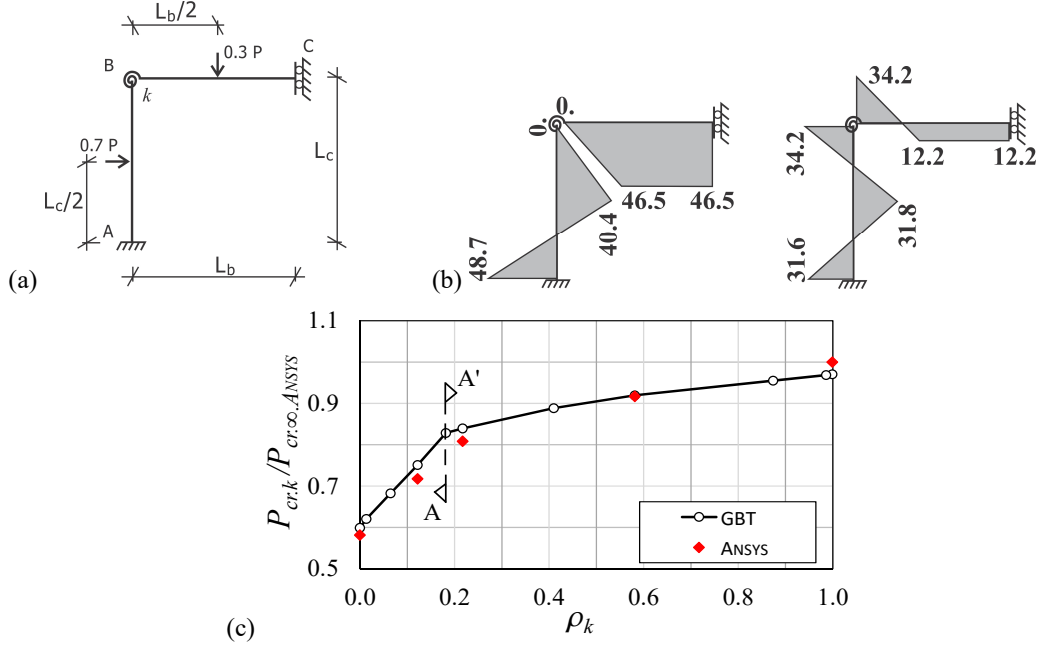
Figure 17: (a) L-shaped frame with a semi-rigid joint, (b) bending moment diagrams (kN.cm) of the pinned and rigid frames, and (c) variation of $P_{cr.k}/P_{cr.\infty}$ with ρ_k

beam has a sliding clamped support and the two are connected by a joint of stiffness k. The loading consists of two concentrated forces applied at the column (*0.7P*) and beam (*0.3P*) mid-span cross-section shear centers. Like the portal frames analyzed earlier, (i) the L-shaped frame exhibits in-plane behavior associated with major-axis flexure (members subjected to axial compression and major-axis bending) and (ii) the variation of ρ_k alters considerably the column and beam bending moment diagrams – Fig. 17(b) shows the bending moment diagrams of frames with a pinned and a rigid joint.

Table 2 shows the critical buckling loads obtained from the GBT ($P_{cr.k.GBT}$) and ANSYS ($P_{cr.k.ANSYS}$) analyses for various ρ_k values as well as the ratio between them ($\Delta_{cr.k}=P_{cr.k.GBT}/P_{cr.k.ANSYS}$) and the nature of the associated buckling modes. Moreover, the values of the normalized joint stiffness, kL_b/EI, are also given. In addition, Fig. 17(c) plots the variation of the semi-rigid frame critical buckling load $P_{cr.k}$, normalized with respect to $P_{cr.\infty.ANSYS}$, with the fixity factor $\rho_k=1/(1+4EI/kL_b)$, and Figs. 18(a)-(d) to 20(a)-(d) show the ANSYS and GBT critical buckling mode shapes of frames with a rigid ($\rho_k=1$), pinned ($\rho_k=0$) and semi-rigid ($\rho_k=0.18$) joint, respectively. As before, each figure shows (i) overall views of the frame critical

Table 2: Buckling results concerning the L-shaped frame (loads in kN)

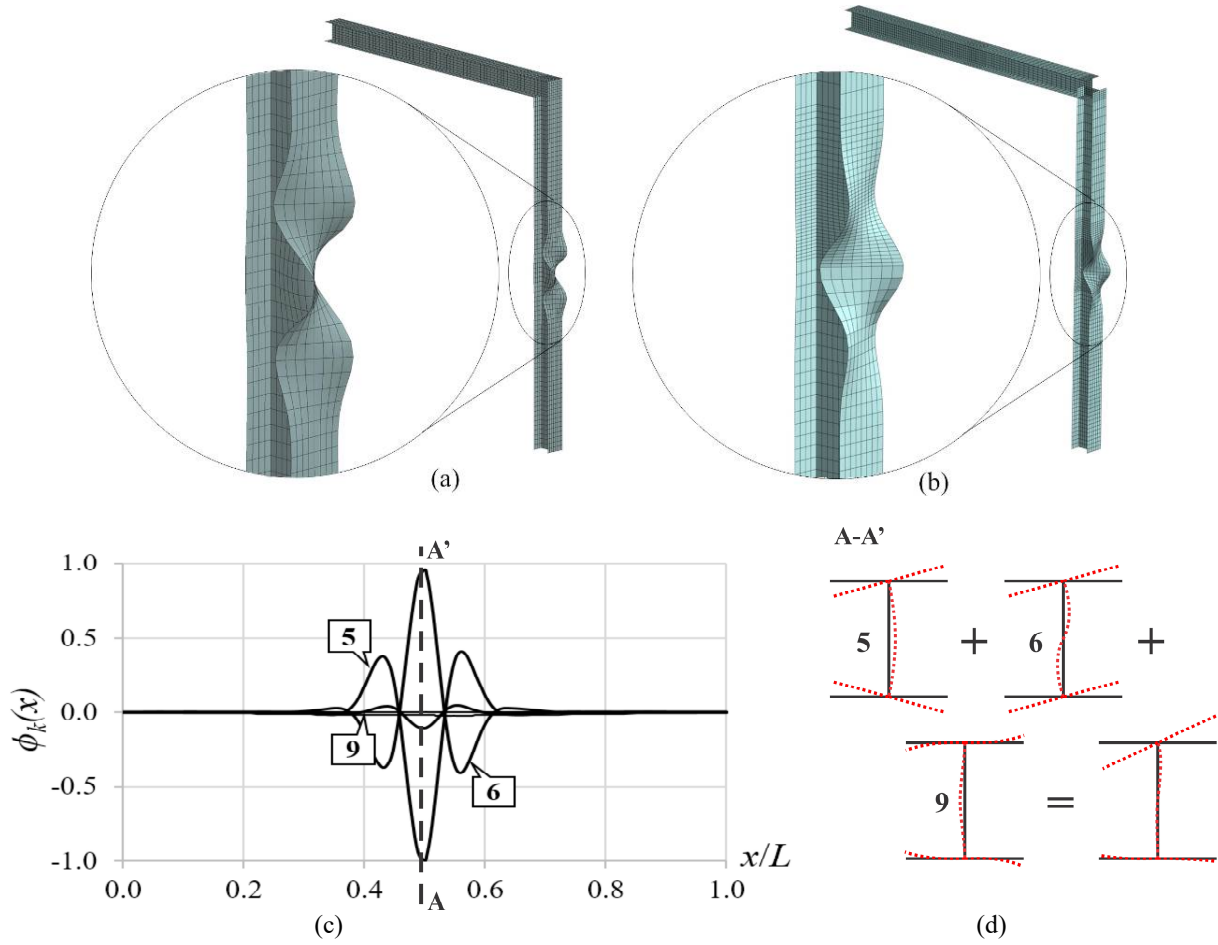| ρ_k	$k_r L_b /EI$	$P_{cr.k.GBT}$	$P_{cr.k.NSYS}$	*Mode nature*	$\Delta_{cr.k}(\%)$
1.00	5200	63.78	65.73	L (column)	0.97
0.99	260	63.66	-	L (column)	-
0.87	26	62.77	-	L (column)	-
0.58	5.0	60.45	60.28	L (column)	1.00
0.41	2.6	58.4	-	L (column)	-
0.22	1.0	55.19	53.15	L (column)	1.04
0.18	0.8	54.45	-	L (column)	-
0.12	0.5	49.38	47.17	L (beam)	1.05
0.06	0.3	44.85	-	L (beam)	-
0.01	0.1	40.8	-	L (beam)	-
0.00	0.0	39.37	38.22	L (beam)	1.03

21

Figure 18: L-shaped frame with a rigid joint: (a) ANSYS and (b) GBT views of the critical buckling mode shape, (c) GBT modal amplitude functions of the beam at buckling and (d) corresponding most deformed cross-section modal decomposition

buckling mode provided by the ANSYS and GBT analyses (including blow-ups of the buckled region), (ii) the GBT deformation mode amplitude functions of the member triggering the frame instability, concerning the frame critical buckling, and (iii) a GBT modal decomposition of the most deformed cross-section of that same member (identified by a dashed line in the plot providing the modal amplitude functions)[8]. The observation and analysis of the buckling results presented in Table 2 and Figures 17 to 20 make it possible to draw the following conclusion:

(i) Once more, there is a virtual coincidence between the critical buckling loads provided by the GBT and ANSYS analyses – the maximum difference is now 5% (except for ρ_k=1, the $P_{cr.k.GBT}$ values are always higher). In addition, there is again an enormous similarity between the three pairs of GBT and ANSYS critical buckling mode representations (see Figs. 18(c)-20(c)).

(ii) Both the rigid and pinned frames exhibit critical local (L) buckling modes, triggered by the column (mid-span region) and beam (half close to the support), respectively. In GBT terms, the buckling of these two frames is governed by the local deformation modes **5**, **6** and **9** – see Figs. 3(d), 18(c)-(d)

---

[8] The GBT buckling analyses of these frames included the first 10 deformation modes depicted in Fig. 3(d) and involved column and beam longitudinal discretizations into 20 beam finite elements,. Note also that the ANSYS shell finite element analyses were performed similarly to those of the portal frames analyzed earlier, *i.e.*, adopting the same "artificial" approach for the semi-rigid frame.
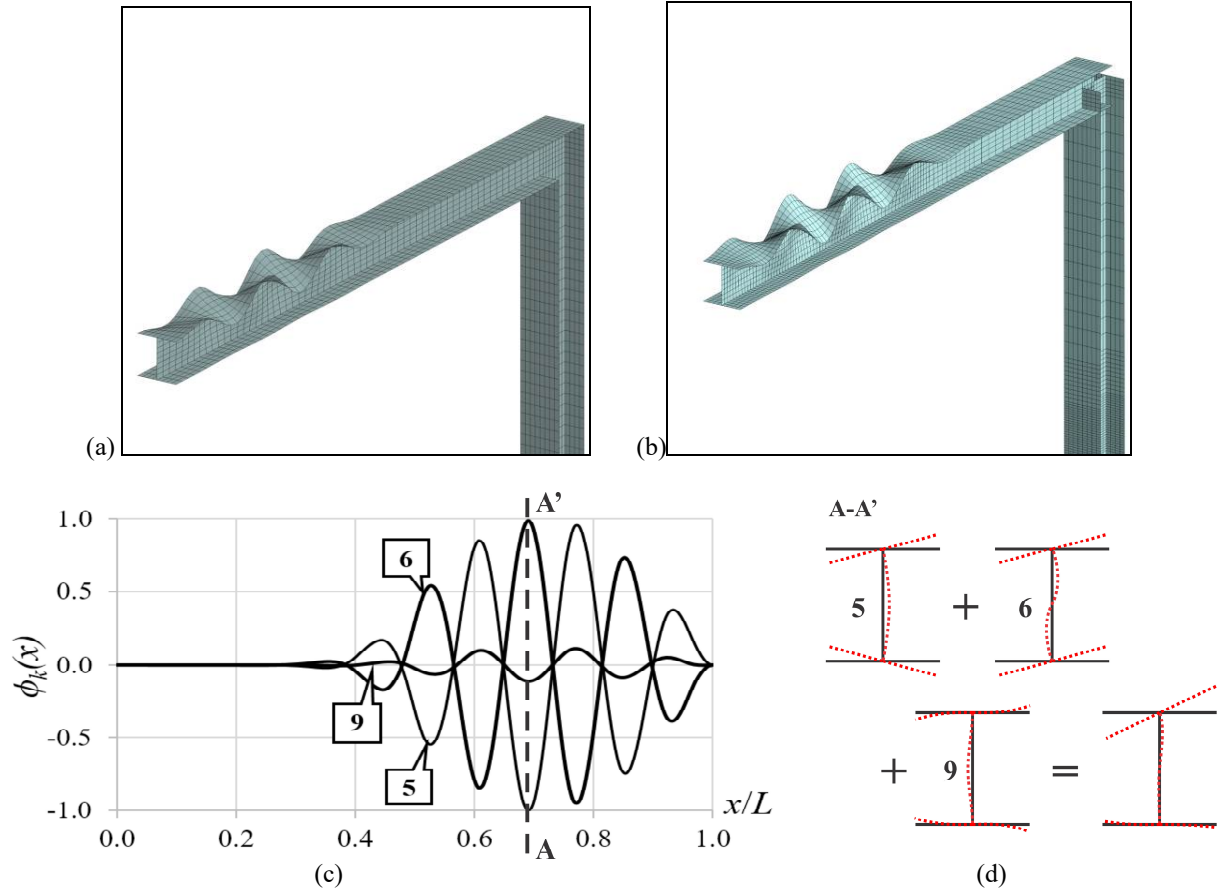
Figure 19: L-shaped frame with a pinned joint: (a) ANSYS and (b) GBT views of the critical buckling mode shape, (c) GBT modal amplitude functions of the beam at buckling and (d) corresponding most deformed cross-section modal decomposition

and 19(c)-(d). As for the semi-rigid frame whose buckling results are depicted in Fig. 20 (ρ_k=0.18), its critical buckling mode combines deformations in the column and beam (like in the ρ_k=0.39 portal frame analyzed earlier) – see Figs. 20(b)-(c).

(iii) The variation of the joint stiffness has a very significant impact on the member bending moment diagrams (see Figure 17(a)) and, like in the portal frame, changes the member triggering the frame instability – for instance, while the buckling of the rigid frame is governed by the column, the pinned frame instability is triggered by the beam. In the particular case of the semi-rigid frame shown in Fig. 20 (ρ_k=0.18), the instability is triggered by the column mid-span region (like in the rigid frame).

(iv) Since critical buckling modes of the rigid and pinned frames (both local) are triggered by the column and beam, respectively, there is certainly a change in the member triggering the frame instability for an intermediate ρ_k value. This value, identified in Fig. 17(c) by the dashed line A-A', is ρ_k=0.18 (note that the semi-rigid frame with ρ_k=0.12 buckles in a L mode triggered by the beam).

(v) Fig. 17(c) shows that, like in the portal frame, the relationship between $P_{cr.k}$ and ρ_k is approximately bi-linear – the transition between the two linear segments corresponds to the change in the member triggering the frame instability. The slope of the first segment is significantly higher than that of the second segment, which means that the joint stiffness affects the beam buckling behavior the most.

(vi) As in the case of the portal frames analyzed before, for most of the joint semi-rigidity range, the frame critical buckling mode shape exibits deformations only in the column (higher ρ_k values) or the
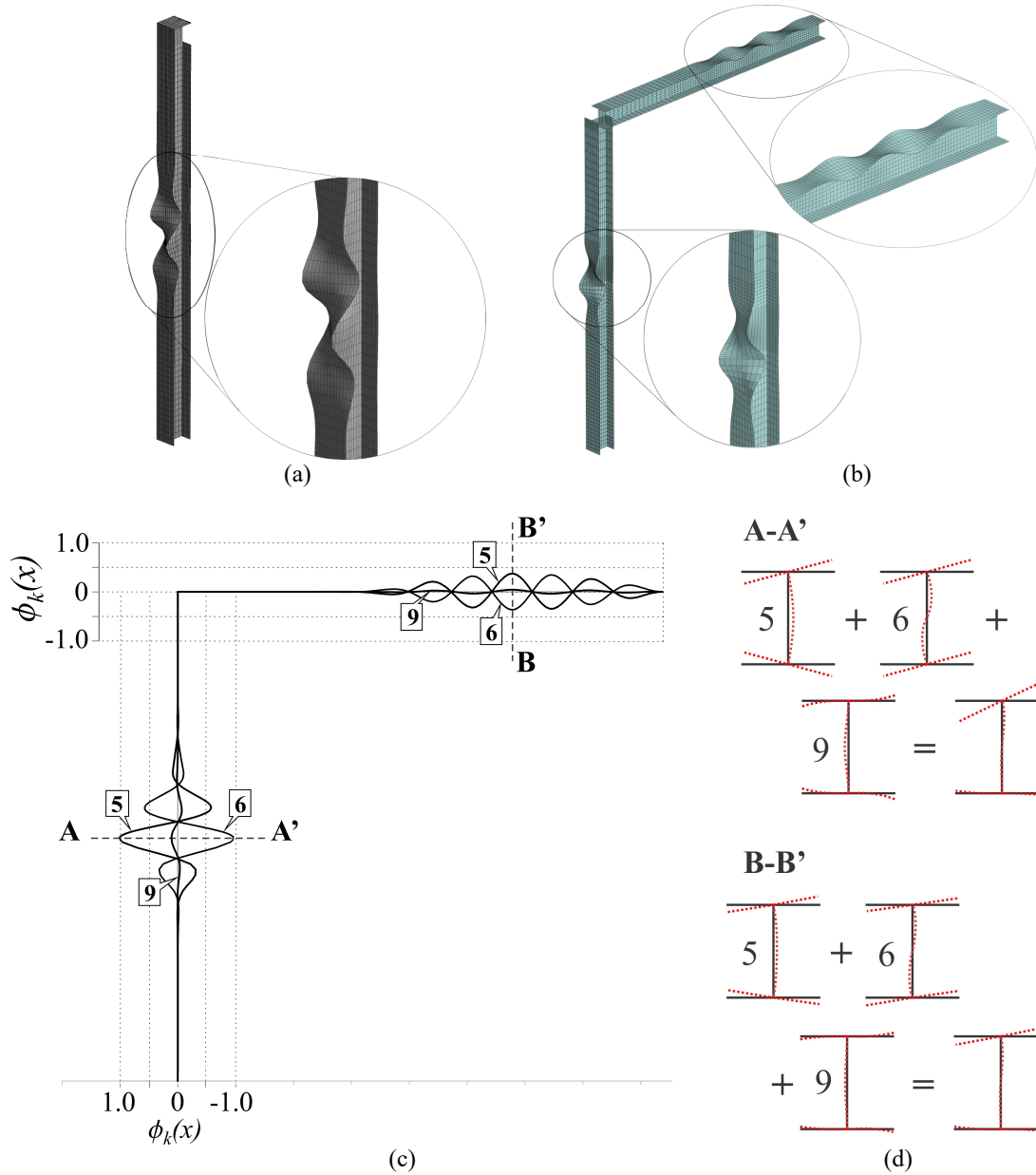
Figure 20: Semi-rigid L-shaped frame (ρ_k=0.18): (a) ANSYS and (b) GBT views of the critical buckling mode shape, (c) GBT modal amplitude functions of the beam at buckling and (d) corresponding most deformed cross-section modal decomposition

beam (lower ρ_k values). However, in frames with ρ_k close to the transition ($\rho_k \approx 0.18$), deformations in both the column and beam occur at critical buckling. For instance, the ρ_k=0.18 frame buckles in a mode involving deformations in the column (dominant) and beam (non-negligible) – see Fig. 20(b).

4. Conclusion

This paper reported the available results of an ongoing investigation on the use of GBT to analyze the local, distortional and global buckling behavior of thin-walled steel frames with semi-rigid joints. After presenting an overview about the performance GBT frame buckling analyses, particular attention was devoted to the aspects related to ensuring displacement compatibility at the frame joints. Next, as a first

attempt to simulate a frame joint semi-rigidity, linear spring elements were incorporated into the buckling analysis − such elements relate generalized displacements of the connected member end cross-sections and are characterized by their stiffness values. Finally, the paper concluded with the presentation and discussion of illustrative numerical results, aimed at providing validation (through the comparison with values obtained from available analytical expressions or ANSYS shell finite element analyses) and showing the capabilities of the proposed approach. These results dealt with the buckling behavior of simple portal and L-shaped plane frames (i) formed by plain and lipped I-section members, respectively, (ii) acted by loadings causing axial compression and in-plane (major-axis) bending, and (iii) exhibiting rotational springs at the joints (involving exclusively in-plane bending. The influence of the spring stiffness (joint semi-rigidity) on the frame buckling behavior (critical buckling load and mode nature) was studied. It was shown that such influence is felt in two different ways, namely the frame (i) pre-buckling axial compression and bending moment (mostly) diagrams, and (ii) buckling eigenvalue problem.

Although there was an excellent correlation between the GBT and ANSYS buckling results presented in the paper (the critical buckling loads never differed by more than 5% and the critical buckling mode shapes were virtually identical), it must be acknowledged that "true comparisons" were only made for (i) portal frames buckling in global modes (the ANSYS results stemmed from beam finite element models) and (ii) portal and L-shaped frames with rigid or pinned joints. In other words, "true comparisons" did not cover the frames with semi-rigid joint buckling in modes involving local and/or distortional deformations. For such frames, the ANSYS shell finite element analyses were performed "artificially", due to the fact that no way was found to incorporate linear springs involving only major-axis flexure (deformation mode **2**) in the shell finite element model. Therefore, because it was found that, in all cases, the frame instability is triggered far from the joint regions, the columns and beams were analyzed separately/individually, (i) acted by the axial force and bending moment diagrams obtained from the semi-rigid frame pre-buckling analysis and (ii) with simple end supports (allowing for torsional rotations). Obviously, this procedure is unable to capture the influence of the joint semi-rigidity (linear springs) on the buckling eigenvalue problem. However, since the GBT buckling analyses (and also the ANSYS ones of the frames with rigid and pinned joints) showed that the contribution of the frame joint regions to the critical buckling mode is imperceptible, it seems fair to argue that the above procedure leads to reasonably accurate frame critical buckling loads, thus making the validation of (comparison with) the GBT values meaningful.

Finally, one last word to mention that the next step of this ongoing research consists of efforts considering commonly used (realistic) semi-rigid joints and determining their stiffness values by means of either the "Component Method" prescribed in Eurocode 3 – Part 1-8 (CEN 2005) or sophisticated numerical models, involving the use of shell/solid finite elements models and contact formulations. Then, the output of this procedure (spring stiffness values) will be incorporated in the GBT formulation and it will be possible to compare the buckling results obtained with values stemming from a rigorous numerical modeling of the whole frame (including the above joints), thus getting around the validation difficulties mentioned in the previous paragraph.

Acknowledgments

References
AISI (American Iron and Steel Institute) (2012). *North American Specification* (NAS) *for the Design of Cold-Formed Steel Structural Members*, AISI-S100-12, Washington DC.

Basaglia C, Camotim D, Silvestre N (2008). Global buckling analysis of plane and space thin-walled frames in the context of GBT, *Thin-Walled Structures*, **46**(1), 79-101.

Basaglia C, Camotim D, Silvestre N (2009). GBT-based local, distortional and global buckling analysis of thin-walled steel frames, *Thin-Walled Structures*, **47**(11), 1246-1264.

Basaglia C, Camotim D, Silvestre N (2010). GBT-based buckling analysis of thin-walled steel frames with arbitrary loading and support conditions, *International Journal of Structural Stability and Dynamics*, **10**(3), 363-385.

Basaglia C, Camotim D, Silvestre N (2012). Torsion warping transmission at thin-walled frame joints: kinematics, modelling and structural response, *Journal of Constructional Steel Research*, **69**(1), 39-53.

Basaglia C, Camotim D (2011). GBT-based buckling analysis of cold-formed steel trusses, *Proceedings of 6th International Conference on Thin-Walled Structures – Recent Research Advances and Trends* (ICTWS 2011 – Timisoara, 5-7/9), D. Dubina, V. Ungureanu (eds.), ECCS (Brussels), 149-156 (vol. 1).

Basaglia C, Camotim D (2015). Buckling analysis of thin-walled steel structural systems using Generalised Beam Theory (GBT), *International Journal of Structural Stability and Dynamics*, 15(1), 1540004:1-28.

Bebiano R, Silvestre N, Camotim D (2007). GBT formulation to analyze the buckling behavior of thin-walled members subjected to non-uniform bending, *International Journal of Structural Stability and Dynamics*, **7**(1), 23-54.

Camotim D, Silvestre N, Basaglia C, Bebiano R (2008). GBT-based buckling analysis of thin-walled members with non-standard support conditions. *Thin-Walled Structures*, **46**(7-9), 800-815.

Camotim D, Basaglia C, Silvestre N (2010). GBT buckling analysis of thin-walled steel frames : A state-of-the-art report, *Thin-Walled Structures*, **48**(10-11), 726-743.

CEN (Comité Européan de Normalisation) (2005). *Eurocode 3: Design of Steel Structures – Part 1.8: Design of Joints*, EN 1993-1-8:2005, Brussels.

Chajes A (1974). *Principles of Structural Stability Theory*, Prentice Hall, Inc. (Englewood Cliffs).

Dinis PB, Camotim D, Silvestre N (2006). GBT formulation to analyse the buckling behaviour of thin-walled members with arbitrarily "branched" open cross-sections, *Thin-Walled Structures*, **44**(1), 20-38.

Dubina D (2008). Structural analysis and design assisted by testing of cold-formed steel structures, *Thin-Walled Structures*, **46**(7-9), 741-764.

Monforton GR, Wu TS (1963). Matrix analysis of semi-rigidly connected frames, *Journal of the Structural Division* (ASCE), **89**(6), 13-42.

Morrell PJB, Riddington JR, Ali FA, Hamid HA (1996). Influence of joint detail on the flexural/torsional interaction of thin-walled structures. *Thin-Walled Structures*, **24**(2), 97-111.

Rasmussen KJR, Zhang X, Zhang H (2016). Beam-element-based analysis of locally and/or distortionally buckled members: theory, *Thin-Walled Structures*, **98B**(January), 285-292.

SAS (Swanson Analysis Systems Inc.) (2009). *Ansys Reference Manual* (version 12).

Sharman PW (1985). Analysis of structures with thin-walled open sections, *International Journal of Mechanical Sciences*, **27**(10), 665-677.

Shayan S, Rasmussen KJR (2014). A model for warping transmission through joints of steel frames, *Thin-Walled Structures*, **82**(September), 1-12.

Silvestre N, Camotim D (2002). First-order generalised beam theory for arbitrary orthotropic materials, *Thin-Walled Structures*, **40**(9), 755-789.

Trahair NS (1993). *Flexural-Torsional Buckling of Structures*, E & FN Spon, London.

Zhang X, Rasmussen KJR (2014). Tests of cold-formed steel portal frames with slender sections. *Steel Construction*, **7**(3), 199-203.

Zhang X, Rasmussen KJR, Zhang H (2015a). Beam-element-based analysis of locally and/or distortionally buckled members: Application, *Thin-Walled Structures*, **95**(October), 127-137.

Zhang X, Rasmussen KJR, Zhang H (2015b). Structural modeling of cold-formed steel portal frames, *Structures*, **4**(November), 58-68.